Thermo-mechanical analysis of laminated composites shells exposed to fire

R. Pacheco[a,b,*], D. Di Capua[a,b], J. Garcia-Espinosa[a,b], O. Casals[c] and T. Hakkarainen[d]

[a] *International Center for Numerical Methods in Engineering (CIMNE), Gran Capitán s/n, 08034 Barcelona, Spain*
[b] *Polytechnic University of Catalonia (UPC), Barcelona, Spain*
[c] *Compass Ingeniería y Sistemas S.A., Spain*
[d] *VTT Technical Research Centre of Finland Ltd, Finland*

ARTICLE INFO

Keywords:
Fire Safety, Fire Collapse, Thermal, Thermomechanical, Damage Constitutive Model, FIBRESHIP project, Composite Materials, SPROM, Rule of Mixtures, Marine Structures

ABSTRACT

This paper describes the research performed within the scope of H2020 project FIBRESHIP in the development and validation of a thermo-mechanical model to assess the fire performance of composite structures. A one-dimensional thermal model with pyrolisis is used to obtain the temperature prole across the thickness and later introduced in the thermomechanical model with a quadrilateral shell element approach. The composite constitutive model employed is the so-called Serial/Parallel Rule of Mixtures (SPROM) which has been modied to introduce the effect of the thermal deformation. A set of experimental tests are then used to validate the correctness of the numerical method proposed. The experimental data used to validate the thermal model is the classic Henderson experimental test. The thermomechanical coupling is validated against an original vertical furnace test of a FRP ships bulkhead following on the 2010 FTP Code standards. These validations demonstrate the correctness and accuracy of the proposed decoupled thermo-mechanical formulation.

1. Introduction

Fibre Reinforced Polymers are extensively used today for building the hull structure of crafts with lengths up to about 50 m. In fact, today most of the pleasure crafts and sailing yachts, passenger and car ferries, patrol and rescue crafts, and naval ships below 50 m length are built in composites. These materials are also used in large secondary structures, but only a few complete units above 50 m length – naval vessels – have been built in composite materials.

The main reason for this limitation in the use of composites is the obligation to use '*steel equivalent*' structural materials to fulfil the fire-safety requirements of the Convention for the Safety of Life at Sea (SOLAS). However, today there is no question that alternative designs with suitable risk control and the use of fire retardant resins, intumescent coatings, fire insulation and active fire-fighting systems can allow FRP structures to fulfil the strictest fire safety regulations. In addition, despite the fact that many polymer composites are flammable, these materials have other properties that may be beneficial in the event of a fire scenario and that are not present in metals. Composites have a heat conduction rate much slower than metals. This fact is translated into a slowdown in the speed of fire spread between rooms and therefore the composite laminate constitutes a very effective barrier against the spread of fire.

These advantages were demonstrated in the large fires on two all-composite minehunter ships operated by the Royal Navy - HMS Ledbury and HMS Cattistock. In both ships, the fire started in the engine/machinery room and in the case of HMS Cattistock the fire burned for over four hours before being extinguished. The fires extensively damaged the compartment of both ships, with the composite hull and bulkheads being heavily charred. However, the low thermal conductivity of the composite bulkheads and decks stopped the fire from spreading by heat conduction to surrounding

*Corresponding Author : R. Pacheco
rafael.pacheco@cimne.upc.edu (R. Pacheco); dicapua@cimne.upc.edu (D. Di Capua); julio@cimne.upc.edu (J. Garcia); ovidi.casals@compassis.com (O. Casals); Tuula.Hakkarainen@vtt.fi (T. Hakkarainen)
www.cimne.com (R. Pacheco); www.compassis.com (O. Casals); www.vttresearch.com (T. Hakkarainen)
ORCID(s):

compartments, which is more difficult to stop in steel ships[1]. Above reasons justify why composite materials are commonly used as thermal insulator of space crafts for the re-entry process.

This work relates to the H2020 project FIBRESHIP, which main objective has been to develop the knowledge and technology required to enable the building of the complete hull and superstructure of large-length ships in composited. This paper describes the research performed within the scope of H2020 project FIBRESHIP in the development and validation of a thermo-mechanical model to assess the fire performance of composite structures.

Fire in composite materials is a complex phenomenon that involves thermal, chemical, and physical processes that can generate the failure of the laminate structure [2]. The heat flux provided by the fire generates a rise of temperature due to heat conduction. When the temperature of the material reaches a high enough value, chemical reactions (pyrolysis or carbon-silica reactions) begin and the matrix of the composite is decomposed to form gaseous products [3]. These gas products are propagated through the porous structure of the composite by diffusion. This effect generates a reduction of the heat due to conduction. The matrix and fibre components suffer thermal expansion and degradation of its mechanical properties. This process generates a drastic reduction of the stiffness and the strength of the laminate structure, which may provoke its failure.

Several models for the analysis of the distribution of the temperature in laminate composites can be found in the literature . One of the most used models in this field is the one presented by Henderson et al. in [3]. In that paper a 1D transient heat transfer model, which takes into account the pyrolysis and carbon-silica reactions phenomena, is proposed. In [4], in order to take into account the thermochemical expansion and the storage of decomposition gases from the solid material, an extension of the previous model is presented. Other similar 1D models are presented in [5–8]. A more complex approach is presented in [9] where heat diffusion, polymer pyrolysis with associated gas production and convection through the matrix are coupled together .

In the last twenty years several thermomechanical models have been also presented for laminate composites under fire conditions. Gibson et al. analysed in [1] the post-fire mechanical properties of woven glass laminates with several resins using a two-layer mechanical model proposed by Mouritz and Mathys in [10–12]. Feih et al. presented models to calculate the tensile and compressive strength of laminate composites exposed to fire in [13] and [13] respectively. Two models, a thermo-chemical and a thermo-mechanical, were developed by Keller et al. in [14] in order to predict the temperature evolution and strength of slabs subjected to fire conditions. Bai and Keller proposed in [15] a model based on beam theory to analyse time-dependent deflections of cellular FRP slab elements exposed to fire from one side. Zhang et al. presented in [16] a 2D thermomechanical model to predict the mechanical response of rectangular GFRP tubes subjected to one-side ISO-834 fire condition. Shi et al. developed in [17] a 3D thermo-mechanical model which took into account the thermo-chemical decomposition and gas diffusion.

One of the most used techniques to evaluate the constitutive behaviour of unidirectional long fibre-reinforced laminates is the classical mixtures theory (CMT). This theory was developed in 1960 by Green and Naghdi [18] in a simpler version known as rule of mixtures (ROM). The ROM theory assumes that all component materials of the composite have the same strain in all directions (parallel behavior). This theory considers the volume fraction of the each component material but not its morphological distribution. To overcome this limitation, some improvements, have been proposed [19, 20]. A very interesting solution is the so-called serial/parallel mixing theory (SPROM) presented by Rastellini et al. in [20]. The SPROM theory assumes components behave as a parallel material in the fibre alignment direction and as a serial material in the rest of directions.

This paper presents a thermo-mechanical model for the analysis of laminate composite structures exposed to fire. The model combines a 1D trough thickness thermal analysis based on the model proposed by Henderson together with a mechanical model based in 3D shells. The constitutive model used for the mechanical behaviour is based in a modification of the SPROM theory to take into account the dilation thermal strains. The model is implemented numerically with in-house software. Experimental tests have been also carried out to validate the proposed model. A numerical example for the analysis of time-to-failure of a composite laminated structure exposed to fire is also presented.

2. Thermal model

The thermal model proposed to solve the non-linear one-dimensional heat problem with pyrolisis constitutive model is based on the thermal model proposed by [21] in conjunction to the boundary conditions in [22].

The composite subjected to the action of fire is considered as a saturated porous media [23]. This media is composed by two phases: a solid matrix phase and an interconnected porous space phase. The solid matrix phase is a mixture of resin matrix, reinforcement fibres and residues from the decomposition reaction.

Each phase has a fraction associated to its volume such that

$$\phi_i := \frac{\Omega_i}{\Omega} = \frac{\Omega_i}{\Omega_s + \Omega_g} \tag{1}$$

where ϕ_i is the phase volume fraction, Ω is the total domain, Ω_i is the phase domain, Ω_s is the solid domain and Ω_g is the gas domain .

The homogenised density, obtained by the rule of mixtures, is

$$\rho := \phi_s \rho_s + \phi_g \rho_g \tag{2}$$

where ρ is the homogenised density, ρ_s is the solid density and ρ_g is the gas density.

2.1. Governing equation

The governing equation for the thermal model proposed in [3] can be rewritten in the following manner

$$\rho C_p \frac{\partial T}{\partial t} = \nabla \cdot (k \nabla T) - \mathbf{w_g} C_{p_g} \nabla T - \frac{\partial \rho}{\partial t}(Q_p + h_s - h_g) \tag{3}$$

where C_p is the specific heat capacity, T is the temperature, k is the through-thickness thermal conductivity, h_g is the gas specific enthalpy, $\mathbf{w_g}$ is the gas mass flux, C_{p_g} is the gas specific heat capacity, Q_p is the polymer degradation energy source and h_s is the solid specific enthalpy.

The mass balance in Equation 3 for each one of the phases is

$$\frac{\partial \phi_s \rho_s}{\partial t} = -\dot{m}_{s \to g} \tag{4}$$

$$\frac{\partial \phi_g \rho_g}{\partial t} = -\nabla \cdot (\mathbf{w_g}) + \dot{m}_{s \to g} \tag{5}$$

where $\dot{m}_{s \to g}$ is the mass flux rate. Equation 4 implies no mass flux ($\mathbf{w_s} = 0$) of the solid phase.

2.1.1. Pyrolisis model

In [3] the decomposition of the solid phase to gas phase is obtained by a linear interpolation relationship between the virgin and degraded states

$$F = \frac{\rho_s - \rho_f}{\rho_0 - \rho_f} \quad \Longleftrightarrow \quad \rho_s = F\rho_0 + (1 - F)\rho_f \tag{6}$$

where F is the degradation fraction, ρ_0 is the virgin density and ρ_f is the char density. The evolution law for the degradation parameter (F) is defined by an nth order Arrhenius equation

$$\begin{gathered} \frac{\mathrm{d}F}{\mathrm{d}t} = -A_T \Big(\frac{\rho_s - \rho_f}{\rho_0 - \rho_f} \Big)^{n_r} \mathrm{e}^{-\frac{E_a}{RT}} \\ \Downarrow \\ \frac{\partial \rho}{\partial t} = (\rho_0 - \rho_f) \frac{\mathrm{d}F}{\mathrm{d}t} \end{gathered} \tag{7}$$

where A_T is the pre-exponential factor for decomposition reaction of polymer matrix, n_r is the order of the decomposition reaction of the polymer matrix, E_a is the activation energy for decomposition reaction of polymer matrix and R is the universal gas constant.

2.1.2. Gas transfer model

Assuming negligible accumulation of gas ($\partial(\phi_g \rho_g)/\partial t = 0$) [3], it can then be concluded that from Equation 4 and Equation 5

$$\nabla \cdot \mathbf{w_g} = \dot{m}_{s\to g} = -\frac{\partial \rho}{\partial t} \tag{8}$$

The gas is assumed to not escape through the cold face of the composite ($\mathbf{w_g}(l_t, t) = 0$), the mass flux field in the gas phase ($\mathbf{w_g}(x, t)$) is calculated in the following manner

$$\int_x^{l_t} \frac{\partial (w_g)}{\partial x}\, \mathrm{d}x = w_g(l_t, t) - w_g(t, x) = -\int_x^{l_t} \frac{\partial \rho}{\partial t} dx \Rightarrow w_g(x, t) = \int_x^{l_t} \frac{\partial \rho}{\partial t} dx \tag{9}$$

Note that in Equation 9, the equivalence $\nabla \cdot \mathbf{w_g} \equiv \partial(w_g)/\partial x$ was introduced were w_g is the first component of the vector $\mathbf{w_g}$. l_t is the thickness of the composite. Equation 9 imposes the direction on which the gas can flow, which is from the cold face to the hot face. This assumption presents instability when the temperature in the cold and hot faces are similar.

2.2. Conditions

2.2.1. Boundary conditions

The boundary conditions are defined similarly to [22], the concept of adiabatic surface temperature – assuming a perfectly insulated surface exposed to radiation and convection – is employed for the hot face

$$q(t, 0) = (-k\boldsymbol{\nabla}\mathbf{T}) \cdot \mathbf{n} = \sigma_\beta \epsilon \Big(T_{ad,k}^4 - T_k^4 \Big) + h_{conv} \Big(T_{ad} - T \Big) \tag{10}$$

and assuming opposite heat flux direction in the cold face as

$$q(t, l) = (-k\boldsymbol{\nabla}\mathbf{T}) \cdot \mathbf{n} = \sigma_\beta \epsilon \Big(T_{\infty,k}^4 - T_k^4 \Big) + h_{conv} \Big(T_\infty - T \Big) \tag{11}$$

where q is the normal heat flux component, $\mathbf{n}$ is the normal, σ_β is the Stefan-Boltzmann constant, ϵ is the emissivity, $T_{ad,k}$ is the adiabatic hot face temperaturei n Kelvin, T_{ad} is the adiabatic hot face temperaturei n Celsius, h_{conv} is the convection coefficient, $T_{\infty,k}$ is the ambient temperaturei n Kelvin and T_∞ is the ambient temperaturei n Celsius.

The boundary conditions expressed in Equation 10 and Equation 11 from [22] can be generalised in this manner

$$q = (-k\boldsymbol{\nabla}\mathbf{T}) \cdot \mathbf{n} = \Big(\sigma_\beta \epsilon (\bar{T}_k^4 - T_k^4) + h_{conv} (\bar{T} - T) \Big) \tag{12}$$

where $\bar{T}$ is the prescribed temperature, which is either, the adiabatic temperature of the hot (T_{ad}) or cold (T_∞) faces. The subscript k denotes the temperature in Kelvin units rather than Celsius.

2.2.2. Initial conditions

Applying ordinary initial conditions to Equation 3

$$\rho(t = 0) = \rho_0, \quad \forall \Omega \tag{13}$$

$$T(t = 0) = T_0, \quad \forall \Omega \tag{14}$$

where T_0 is the virgin temperature. Note that in the present research, the ambient temperature and initial/virgin temperature are assumed to be the same.

2.3. Weak form

Using the relationship from Equation 9, the mass flux ($\mathbf{w_g}$) can be found. Thus the weak form of the problem can be obtained by applying the method of mean weighted residuals in Equation 3.

$$\begin{aligned}\int_\Omega \xi\rho C_p\frac{\partial T}{\partial t}\,\mathrm{d}\Omega + \int_\Omega \nabla\xi k\nabla T\,\mathrm{d}\Omega + \int_\Omega \xi C_{p_g}\mathbf{w_g}\nabla T\,\mathrm{d}\Omega + \int_\Omega \xi(\rho_0-\rho_f)\frac{\mathrm{d}F}{\mathrm{d}t}(Q_p+h_s-h_g)\,\mathrm{d}\Omega \\ + \int_{\partial\Omega}\xi\Big(\sigma_\beta\epsilon(\bar{T}_k^4-T_k^4)+h_{conv}(\bar{T}-T)\Big)\,\mathrm{d}\Gamma = 0\end{aligned} \tag{15}$$

where ξ is the test function and $(\partial\Omega)$ refers to the domain boundary, which arises from applying the divergence theorem to the divergence term that appears from the substitution of the integration by parts of the Laplacian term.

2.4. Finite element discretisation

The temperature field can be discretised using the interpolation shape functions

$$T(x,t) = \mathbf{NT} \equiv \begin{bmatrix}N_1 & \dots & N_{n_{\text{nodes}}}\end{bmatrix}\begin{bmatrix}T_1 & \dots & T_{n_{\text{nodes}}}\end{bmatrix}^T \tag{16}$$

where $\mathbf{N}$ is the nodal shape function matrix, $\mathbf{T}$ is the nodal temperature vector and (n_{nodes}) is the total number of nodes. By using the standard Galerkin method the Equation 15 can be written as

$$\mathbf{C_T}\frac{\partial \mathbf{T}}{\partial t} + \mathbf{K_T}\mathbf{T} - (\mathbf{q_d}+\mathbf{q_c}+\mathbf{q_r}) = \mathbf{0} \tag{17}$$

where

$$\mathbf{C_T} = \sum_e\left(\int_\Omega \rho C_p\mathbf{N}^T\mathbf{N}\,\mathrm{d}\Omega\right), \quad \forall i\in 1,...,n_{\text{elm}} \tag{18}$$

$$\mathbf{K_T} = \sum_e\left(\int_\Omega k\boldsymbol{\nabla}\mathbf{N}^T\boldsymbol{\nabla}\mathbf{N}\,\mathrm{d}\Omega\right) = \sum_e\left(\int_\Omega k{\mathbf{B_T}}^T\mathbf{B_T}\,\mathrm{d}\Omega\right), \quad \forall i\in 1,...,n_{\text{elm}} \tag{19}$$

$$\mathbf{q_d} = -\sum_e\left(\int_\Omega \mathbf{N}^T(\rho_0-\rho_f)\frac{\mathrm{d}F}{\mathrm{d}t}(Q_p+h_s-h_g)\,\mathrm{d}\Omega\right) - \sum_e\left(\int_\Omega \mathbf{N}^T C_{p_g}\mathbf{w_g}\boldsymbol{\nabla}\mathbf{T}\,\mathrm{d}\Omega\right), \quad \forall i\in 1,...,n_{\text{elm}} \tag{20}$$

$$\mathbf{q_c} = -\sum_e\left(\int_{\partial\Omega}\mathbf{N}^T h_{conv}(\bar{T}-T)\,\mathrm{d}\Gamma\right), \quad \forall i\in 1,...,n_{\text{elm}} \tag{21}$$

$$\mathbf{q_r} = -\sum_e\left(\int_{\partial\Omega}\mathbf{N}^T\sigma_\beta\epsilon(\bar{T}^4-T_k^4)\,\mathrm{d}\Gamma\right), \quad \forall i\in 1,...,n_{\text{elm}} \tag{22}$$

being (n_{elm}) the total number of elements, $\mathbf{C_T}$ is the specific heat matrix, $\mathbf{K_T}$ is the conductivity matrix, $\mathbf{B_T}$ is the gradient matrix, $\mathbf{q_d}$ is the degraded heat flux vector, $\mathbf{q_c}$ is the convection heat flux vector, $\mathbf{q_r}$ is the radiation heat flux vector.

2.5. Time integration and non-linear solution strategy

The time is discretised in non-overlapping subintervals $\sum_n(t_{n+1}-t_n)$ and by using a backward-Euler scheme, Equation 17 can be written as

$$\mathbf{r_T}\big|_{n+1} \equiv \mathbf{r_T}(T_{n+1},F_{n+1}) = \mathbf{C_T}\big|_{n+1}\left(\frac{\mathbf{T}|_{n+1}-\mathbf{T}|_n}{\Delta t}\right) + \mathbf{K_T}\big|_{n+1}\,\mathbf{T}|_{n+1} - (\mathbf{q_d}\big|_{n+1}+\mathbf{q_c}\big|_{n+1}+\mathbf{q_r}\big|_{n+1}) = \mathbf{0} \tag{23}$$

where $\mathbf{r_T}$ is the residual heat flux vector. Equation 23 represents a non-linear problem which depends of the state variable (T) and the internal variable (F) . To solve this problem the Newton-Raphson method can be applied, the solution can be summarised in the algorithm 1.

3. Mechanical model

The mechanical behavior of composite materials structure is analysed using the serial/parallel mixing theory [20]. In the present article, the capabilities of the so-called serial/parallel rule of mixtures – in short SP-RoM – have been extended for composites exposed to high temperatures. The constitutive mechanical model proposed in this work is developed based on Reissner-Mindlin flat shell theory [24, 25], where $\boldsymbol{\varepsilon} := [\varepsilon_x, \varepsilon_y, \gamma_{xy}, \gamma_{yz}, \gamma_{zx}]^T$ is the mechanical strain vector $\boldsymbol{\sigma} := [\sigma_x, \sigma_y, \tau_{xy}, \tau_{yz}, \tau_{zx}]^T$ and the internal stress, both expressed in Voigt nomenclature.

3.1. Serial-parallel rules of mixing

The SP-RoM acts as a constitutive equation manager, and is capable of successfully predict the structural performance of the composite, taking into account the specific behaviour of the composite in its parallel and serial direction, as well as the non-linearities of the composite components [20]. To do so, the strain vector is split into its parallel and serial components ($\boldsymbol{\varepsilon}_\mathbf{p}$) and ($\boldsymbol{\varepsilon}_\mathbf{s}$) , respectively, using a projector matrix, $\mathbf{P}_\mathbf{p}$. This matrix is obtained using the fibre orientation in the composite. The procedure to perform this decomposition is described as follows

$$\boldsymbol{\varepsilon} \equiv \boldsymbol{\varepsilon}_\mathbf{p} + \boldsymbol{\varepsilon}_\mathbf{s} = \mathbf{P}_{\mathbf{p},\boldsymbol{\varepsilon}}\boldsymbol{\varepsilon} + \mathbf{P}_{\mathbf{s},\boldsymbol{\varepsilon}}\boldsymbol{\varepsilon} \tag{24}$$

$$\boldsymbol{\sigma} \equiv \boldsymbol{\sigma}_\mathbf{p} + \boldsymbol{\sigma}_\mathbf{s} = \mathbf{P}_{\mathbf{p},\boldsymbol{\sigma}}\boldsymbol{\sigma} + \mathbf{P}_{\mathbf{s},\boldsymbol{\sigma}}\boldsymbol{\sigma} \tag{25}$$

where

$$\mathbf{P}_{\mathbf{p},\boldsymbol{\varepsilon}} := \begin{bmatrix} \cos^4(\theta) & \cos^2(\theta)\sin^2(\theta) & \cos^3(\theta)\sin(\theta) & 0 & 0 \\ \cos^2(\theta)\sin^2(\theta) & \sin^4(\theta) & \cos(\theta)\sin^3(\theta) & 0 & 0 \\ 2\cos^3(\theta)\sin(\theta) & 2\cos(\theta)\sin^3(\theta) & 2\cos^2(\theta)\sin^2(\theta) & 0 & 0 \\ 0 & 0 & 0 & 0 & 0 \\ 0 & 0 & 0 & 0 & 0 \end{bmatrix}, \quad \mathbf{P}_{\mathbf{s},\boldsymbol{\varepsilon}} := \mathbf{I} - \mathbf{P}_{\mathbf{p},\boldsymbol{\varepsilon}} \tag{26}$$

$$\mathbf{P}_{\mathbf{p},\boldsymbol{\sigma}} := \begin{bmatrix} \cos^4(\theta) & \cos^2(\theta)\sin^2(\theta) & 2\cos^3(\theta)\sin(\theta) & 0 & 0 \\ \cos^2(\theta)\sin^2(\theta) & \sin^4(\theta) & 2\cos(\theta)\sin^3(\theta) & 0 & 0 \\ \cos^3(\theta)\sin(\theta) & \cos(\theta)\sin^3(\theta) & 2\cos^2(\theta)\sin^2(\theta) & 0 & 0 \\ 0 & 0 & 0 & 0 & 0 \\ 0 & 0 & 0 & 0 & 0 \end{bmatrix}, \quad \mathbf{P}_{\mathbf{s},\boldsymbol{\sigma}} := \mathbf{I} - \mathbf{P}_{\mathbf{p},\boldsymbol{\sigma}} \tag{27}$$

$\boldsymbol{\varepsilon}$ is the strain, $\boldsymbol{\varepsilon}_\mathbf{p}$ is the parallel strain, $\boldsymbol{\varepsilon}_\mathbf{s}$ is the serial strain, $\boldsymbol{\sigma}_\mathbf{p}$ is the parallel stress, $\boldsymbol{\sigma}_\mathbf{s}$ is the serial stress and $\mathbf{P}_{\mathbf{p},\boldsymbol{\varepsilon}}$, $\mathbf{P}_{\mathbf{s},\boldsymbol{\varepsilon}}$, $\mathbf{P}_{\mathbf{p},\boldsymbol{\sigma}}$ and $\mathbf{P}_{\mathbf{s},\boldsymbol{\sigma}}$ are their respective parallel and serial projectors, θ is the fibre orientation in the layer with respect to the element local axis x' described in Figure 1, $\mathbf{I}$ is the identity matrix. Note that the projectors have a different relationship between their Voigt and tensor notations and thus each one has its set of parallel and serial projectors.

Once knowing the parallel and serial components of the composite, it is possible to apply to each one a compatibility conditions that defines how the composite constituents, fibre and matrix, interact between each other:

$$\text{Parallel} \quad \begin{cases} \boldsymbol{\varepsilon}_\mathbf{p} = \boldsymbol{\varepsilon}_\mathbf{p,f} = \boldsymbol{\varepsilon}_\mathbf{p,m} \\ \boldsymbol{\sigma}_\mathbf{p} = \phi_f \boldsymbol{\sigma}_\mathbf{p,f} + \phi_m \boldsymbol{\sigma}_\mathbf{p,m} \end{cases} \tag{28}$$

$$\text{Serial} \quad \begin{cases} \boldsymbol{\varepsilon}_\mathbf{s} = \phi_f \boldsymbol{\varepsilon}_\mathbf{p,f} + \phi_m \boldsymbol{\varepsilon}_\mathbf{p,m} \\ \boldsymbol{\sigma}_\mathbf{s} = \boldsymbol{\sigma}_\mathbf{s,f} = \boldsymbol{\sigma}_\mathbf{s,m} \end{cases} \tag{29}$$

where $\boldsymbol{\sigma}_\mathbf{p,m}$ is the parallel matrix stress, $\boldsymbol{\sigma}_\mathbf{s,m}$ is the serial matrix stress, $\boldsymbol{\sigma}_\mathbf{p,f}$ is the parallel fibre stress, $\boldsymbol{\sigma}_\mathbf{s,f}$ is the serial fibre stress, $\boldsymbol{\sigma}_\mathbf{s}$ is the serial composite stress, $\boldsymbol{\sigma}_\mathbf{p}$ is the parallel composite stress, $\boldsymbol{\varepsilon}_\mathbf{p,m}$ is the parallel matrix strain, $\boldsymbol{\varepsilon}_\mathbf{s,m}$ is the serial matrix strain, $\boldsymbol{\varepsilon}_\mathbf{p,f}$ is the parallel fibre strain, $\boldsymbol{\varepsilon}_\mathbf{s,f}$ is the serial fibre strain, $\boldsymbol{\phi}_\mathbf{m}$ is the matrix volume fraction and $\boldsymbol{\phi}_\mathbf{f}$ is the fibre volume fraction.

Combining Equation 24, Equation 25, Equation 28 and Equation 30, the composite strain and stress yield

$$\begin{cases} \boldsymbol{\varepsilon} = \phi_f \boldsymbol{\varepsilon}_{\mathbf{p,f}} + \phi_m \boldsymbol{\varepsilon}_{\mathbf{p,m}} + \phi_f \boldsymbol{\varepsilon}_{\mathbf{s,f}} + \phi_m \boldsymbol{\varepsilon}_{\mathbf{s,m}} \\ \boldsymbol{\sigma} = \phi_f \boldsymbol{\sigma}_{\mathbf{p,f}} + \phi_m \boldsymbol{\sigma}_{\mathbf{p,m}} + \phi_f \boldsymbol{\sigma}_{\mathbf{s,f}} + \phi_m \boldsymbol{\sigma}_{\mathbf{s,m}} \end{cases} \tag{30}$$

3.2. Constitutive equations of the constituent materials exposed to high temperatures

The constitutive behaviour of matrix and fibre materials are both modelled with isotropic damage models [26]

$$\boldsymbol{\sigma}_{\mathbf{f}} := (1 - d_f)\mathbb{C}_{\mathbf{f}}(\boldsymbol{\varepsilon}_{\mathbf{f}} - \boldsymbol{\varepsilon}_{\mathbf{T,f}}) \tag{31}$$

$$\boldsymbol{\sigma}_{\mathbf{m}} := (1 - d_m)\mathbb{C}_{\mathbf{m}}(\boldsymbol{\varepsilon}_{\mathbf{m}} - \boldsymbol{\varepsilon}_{\mathbf{T,m}}) \tag{32}$$

where σ_m is the matrix stress, σ_f is the fibre stress, ε_m is the matrix strain, ε_f is the fibre strain, d_m is the matrix isotropic damage index, d_f is the fibre isotropic damage index, $\mathbb{C}_m$ is the matrix elastic constitutive tensor, $\mathbb{C}_f$ is the fibre elastic constitutive tensor, $\varepsilon_{T,m}$ is the matrix thermal strain and $\varepsilon_{T,f}$ is the fibre thermal strain.

The thermal strain of each of the constituent materials is anisotropic which is achieved by

$$\boldsymbol{\varepsilon}_{\mathbf{T,i}} := \boldsymbol{\alpha}_{\mathbf{i}} \Delta T = \boldsymbol{\alpha}_{\mathbf{i}} \big(T(x,t) - T(x,0)\big), \quad \forall i \in f, m \tag{33}$$

where α_i is the constituent material thermal expansion coefficienta nd is defined as $\boldsymbol{\alpha} := [\alpha_x, \alpha_y, 0, 0, 0]^T$. Note that i refers to properties associated to the constituent material.

Thus, the elastic constitutive matrix, for Reissner-Mindlin flat shell theory, becomes

$$\mathbb{C}_{\mathbf{i}} := \frac{E_i}{1 - \nu_i^2} \begin{bmatrix} 1 & \nu_i & 0 & 0 & 0 \\ \nu_i & 1 & 0 & 0 & 0 \\ 0 & 0 & \dfrac{1 - \nu_i}{2} & 0 & 0 \\ 0 & 0 & 0 & \dfrac{1 - \nu_i}{2} & 0 \\ 0 & 0 & 0 & 0 & \dfrac{1 - \nu_i}{2} \end{bmatrix}, \quad \forall i \in f, m \tag{34}$$

where E_i is the Young modulus, which is considered dependent from the temperature and the degradation fraction and ν_i is the Poisson ratio that is constant.

In order to define concepts such as loading and unloading for general 3D stress states, it is necessary to define a scalar positive quantity in terms of normalised equivalent stress. This will permit the comparison of different 3D stress states, even for different degrees of thermal degradation.

$$\delta_i = \left(\varsigma + \frac{1 - \varsigma}{\beta_{,i}}\right)\sqrt{E_{0,i}}\sqrt{\frac{\bar{\boldsymbol{\sigma}}_{\mathbf{i}}}{\sigma_{y,i}} : (\mathbb{C}_{\mathbf{0,i}})^{-1} : \frac{\bar{\boldsymbol{\sigma}}_{\mathbf{i}}}{\sigma_{y,i}}}, \quad \forall i \in f, m \tag{35}$$

where $\bar{\sigma}_i$ is the effective stress, δ_i is the damage threshold, ς is the stress weight factor, $\beta_{,i}$ is the compress-traction coefficient, $E_{,i}$ is the initial Young modulus, $\sigma_{y,i}$ is the yield stress, which is considered to be dependent of the temperature and the degradation factor and $\mathbb{C}_{0,i}$ is the initial elastic constitutive tensor.

The effective stress for each constituent material is defined as

$$\bar{\boldsymbol{\sigma}}_{\mathbf{i}} := \mathbb{C}_{\mathbf{i}}(\boldsymbol{\varepsilon}_{\mathbf{i}} - \boldsymbol{\varepsilon}_{\mathbf{T,i}}), \quad \forall i \in f, m \tag{36}$$

The stress weight factor is equivalent to

$$\varsigma_i := \frac{\sum_{k=1}^{3} \left\langle \boldsymbol{\sigma}_{\mathbf{k,i}} \right\rangle}{\sum_{k=1}^{3} \left| \boldsymbol{\sigma}_{\mathbf{k,i}} \right|}, \quad \forall i \in f, m \tag{37}$$

And the compression-traction coefficient is the ratio between the compression and traction yield stress

$$\beta_{,i} := \frac{\sigma_{y,comp,i}}{\sigma_{y,trac,i}}, \quad \forall i \in f, m \tag{38}$$

The evolution of the damage index is controlled by the internal variable, which is defined by Faria et al. in [27]. Thus the definition of the damage index respect the internal variable is

$$d_i(r_i) := \frac{1 - \mathrm{e}^{A_i(1-r_i)}}{r_i}, \quad \text{if } r_i \geq r_{0,i}, \quad \forall i \in f, m \tag{39}$$

where r_i is the normalised internal variable, A_i is the pre-exponential factor of the isotropic damage model, which is a mesh independent parameter by means of the characteristic length as shown in [28] and depends on the size (volume, area or length) of the discretised spatial mesh. The pre-exponential factor can be calculated using [27, 28]

$$A_i = \left(\frac{G_{f,i} E_i}{l_{c,i}\, \sigma_{y,i}^2} - \frac{1}{2} \right), \quad \forall i \in f, m \tag{40}$$

where $l_{c,i}$ is the characteristic length and $G_{f,i}$ is the fracture energy. The fracture energy of each constituent material depends on temperature and degradation factor. Due to the lack of experimental information to characterise the evolution of the fracture energy respect to the temperature and the degradation factor, this evolution is in terms of the Young modulus and the yield stress which depend also on both temperature and degradation factor

$$\frac{G_{f,i} E_i}{\sigma_{y,i}^2} = \text{constant}, \quad \forall i \in f, m \tag{41}$$

The Young modulus (E) and the yield stress (σ_y) follow the evolution law proposed in [29]

$$P_i(T, F) = \left(\frac{P_{u,i} + P_{r,i}}{2} - \frac{P_{u,i} - P_{r,i}}{2} \tanh \chi_{1,i}(T - T_{g,i}) F^{\chi_{2,i}} \right), \quad \forall i \in f, m \tag{42}$$

where (P_u) is the unrelaxed and (P_r) is the relaxed value of a generic property (P), $T_{g,i}$ is the glass transition temperature, $\chi_{1,i}$ is the first Mourtiz and Gibson fitting parameter, $\chi_{2,i}$ is the second Mourtiz and Gibson fitting parameter.

The parameters found in Equation 42 shall be calibrated with experimental tests at high temperatures for each of the constituent materials. However, calibration of composites at high temperatures is regularly done on the composite laminated material as a whole which poses an important problem. In the absence of experimental data for each constituent material, the following relationship can be taken into account

$$\frac{P_r}{P_u} = \frac{P_{r,m}}{P_{u,m}} = \frac{P_{r,f}}{P_{u,f}} \tag{43}$$

$$\chi_1 = \chi_{1,m} = \chi_{1,f} \tag{44}$$

$$\chi_2 = \chi_{2,m} = \chi_{2,f} \tag{45}$$

which establishes a correlation between the evolution of the property (P) for each constituent material and the composite as a whole.

3.3. Constitutive equations of composite materials exposed to high temperatures

Similarly to the approach in [20], Equation 31 and Equation 32 can be written in differential form as

$$\mathrm{d}\boldsymbol{\sigma}_{\mathbf{f}} := \mathbb{C}_{\mathbf{tan,m}} (\, \mathrm{d}\boldsymbol{\varepsilon}_{\mathbf{f}} - \mathrm{d}\boldsymbol{\varepsilon}_{\mathbf{T,f}}) \tag{46}$$

$$\mathrm{d}\boldsymbol{\sigma}_{\mathbf{m}} := \mathbb{C}_{\mathbf{tan,f}}(\,\mathrm{d}\boldsymbol{\varepsilon}_{\mathbf{m}} - \,\mathrm{d}\boldsymbol{\varepsilon}_{\mathbf{T,m}}) \tag{47}$$

where $\mathbb{C}_{\mathbf{tan,m}}$ is the matrix tangent elastic constitutive tensor and $\mathbb{C}_{\mathbf{tan,f}}$ is the fibre tangent elastic constitutive tensor. The serial and parallel decomposition of the internal stress of each constituent material in differential form can be achieved by

$$\mathrm{d}\boldsymbol{\sigma}_{\mathbf{p,i}} := \mathbb{C}_{\mathbf{pp,i}}(\,\mathrm{d}\boldsymbol{\varepsilon}_{\mathbf{p,i}} - \,\mathrm{d}\boldsymbol{\varepsilon}_{\mathbf{T,p,i}}) + \mathbb{C}_{\mathbf{ps,i}}(\,\mathrm{d}\boldsymbol{\varepsilon}_{\mathbf{s,i}} - \,\mathrm{d}\boldsymbol{\varepsilon}_{\mathbf{T,s,i}}), \quad \forall i \in f, m \tag{48}$$

$$\mathrm{d}\boldsymbol{\sigma}_{\mathbf{s,i}} := \mathbb{C}_{\mathbf{sp,i}}(\,\mathrm{d}\boldsymbol{\varepsilon}_{\mathbf{p,i}} - \,\mathrm{d}\boldsymbol{\varepsilon}_{\mathbf{T,p,i}}) + \mathbb{C}_{\mathbf{ss,i}}(\,\mathrm{d}\boldsymbol{\varepsilon}_{\mathbf{s,i}} - \,\mathrm{d}\boldsymbol{\varepsilon}_{\mathbf{T,s,i}}), \quad \forall i \in f, m \tag{49}$$

where

$$\mathbb{C}_{\mathbf{tan,i}} := \begin{bmatrix} \mathbb{C}_{\mathbf{pp,i}} & \mathbb{C}_{\mathbf{ps,i}} \\ \mathbb{C}_{\mathbf{sp,i}} & \mathbb{C}_{\mathbf{ss,i}} \end{bmatrix} \equiv \begin{bmatrix} \dfrac{\partial \boldsymbol{\sigma}_{\mathbf{p,i}}}{\partial \boldsymbol{\varepsilon}_{\mathbf{p,i}}} & \dfrac{\partial \boldsymbol{\sigma}_{\mathbf{p,i}}}{\partial \boldsymbol{\varepsilon}_{\mathbf{s,i}}} \\ \dfrac{\partial \boldsymbol{\sigma}_{\mathbf{s,i}}}{\partial \boldsymbol{\varepsilon}_{\mathbf{p,i}}} & \dfrac{\partial \boldsymbol{\sigma}_{\mathbf{s,i}}}{\partial \boldsymbol{\varepsilon}_{\mathbf{s,i}}} \end{bmatrix} \equiv \begin{bmatrix} \mathbf{P}_{\mathbf{p},\sigma}\mathbb{C}_{\mathbf{tan,i}}\mathbf{P}_{\mathbf{p},\varepsilon} & \mathbf{P}_{\mathbf{p},\sigma}\mathbb{C}_{\mathbf{tan,i}}\mathbf{P}_{\mathbf{s},\varepsilon} \\ \mathbf{P}_{\mathbf{s},\sigma}\mathbb{C}_{\mathbf{tan,i}}\mathbf{P}_{\mathbf{p},\varepsilon} & \mathbf{P}_{\mathbf{s},\sigma}\mathbb{C}_{\mathbf{tan,i}}\mathbf{P}_{\mathbf{s},\varepsilon} \end{bmatrix}, \quad \forall i \in f, m \tag{50}$$

In the SP-RoM theory, the matrix serial strain is selected as an independent internal variable to satisfy Equation 28 and Equation 30. The fibre serial strain can then be expressed as

$$\boldsymbol{\varepsilon}_{\mathbf{s,f}}(\boldsymbol{\varepsilon}_{\mathbf{s,m}}) := \frac{1}{\phi_f}\boldsymbol{\varepsilon}_{\mathbf{s}} - \frac{\phi_s}{\phi_f}\boldsymbol{\varepsilon}_{\mathbf{s,m}} \tag{51}$$

The objective function to minimise is defined from Equation 30 and solved by applying a Newton-Rapshon scheme

$$\left\{ \boldsymbol{\Delta\sigma}_{\mathbf{s}}(\,\boldsymbol{\varepsilon}_{\mathbf{s,m}}\big|_{k+1}) = \boldsymbol{\Delta\sigma}_{\mathbf{s}}(\,\boldsymbol{\varepsilon}_{\mathbf{s,m}}\big|_{k}) + \left.\frac{\partial \boldsymbol{\Delta\sigma}_{\mathbf{s}}}{\partial \boldsymbol{\varepsilon}_{\mathbf{s,m}}}\right|_{k} \boldsymbol{\Delta\varepsilon}_{\mathbf{s,m}}\big|_{k+1} \quad : \quad \boldsymbol{\Delta\sigma}_{\mathbf{s}} := \boldsymbol{\sigma}_{\mathbf{s,m}} - \boldsymbol{\sigma}_{\mathbf{s,f}} = 0 \right\} \tag{52}$$

where the objective function ($\boldsymbol{\Delta\sigma}_{\mathbf{s}}$) is the serial internal stress residue. The Jacobian of the residue can be formulated by using Equation 50 and Equation 51

$$\mathbf{J}|_k := \left.\frac{\partial \boldsymbol{\Delta\sigma}_{\mathbf{s}}}{\partial \boldsymbol{\varepsilon}_{\mathbf{s,m}}}\right|_k = \left.\frac{\partial \boldsymbol{\sigma}_{\mathbf{s,m}}}{\partial \boldsymbol{\varepsilon}_{\mathbf{s,m}}}\right|_k - \left.\frac{\partial \boldsymbol{\sigma}_{\mathbf{s,f}}}{\partial \boldsymbol{\varepsilon}_{\mathbf{s,f}}}\right|_k \left.\frac{\partial \boldsymbol{\varepsilon}_{\mathbf{s,f}}}{\partial \boldsymbol{\varepsilon}_{\mathbf{s,m}}}\right|_k \equiv \mathbb{C}_{\mathbf{ss,m}}\big|_k + \frac{\phi_m}{\phi_f}\,\mathbb{C}_{\mathbf{ss,f}}\big|_k \tag{53}$$

Therefore the updated scheme of the design variable is

$$\boldsymbol{\varepsilon}_{\mathbf{s,m}}\big|_{k+1} = \boldsymbol{\varepsilon}_{\mathbf{s,m}}\big|_k - (\mathbf{J}|_k)^{-1}\boldsymbol{\Delta\sigma}_{\mathbf{s}}(\,\boldsymbol{\varepsilon}_{\mathbf{s,m}}\big|_k) \tag{54}$$

The initial prediction ($k = 0$) is based on the converged serial matrix strain of the previous step. Being

$$\boldsymbol{\varepsilon}_{\mathbf{s,m}}(t + \Delta t)\big|_0 = \boldsymbol{\varepsilon}_{\mathbf{s,m}}(t)\big|_0 + \boldsymbol{\Delta\varepsilon}_{\mathbf{s,m}}\big|_0 \tag{55}$$

This initial prediction can be obtained by assuming that in Equation 49 the serial differential internal stress is the same for both matrix and fibre

$$\begin{gathered} \boldsymbol{\Delta\sigma}_{\mathbf{s,m}} = \boldsymbol{\Delta\sigma}_{\mathbf{s,f}} \\ \Downarrow \\ \mathbb{C}_{\mathbf{sp,m}}(\boldsymbol{\Delta\varepsilon}_{\mathbf{p,m}} - \boldsymbol{\Delta\varepsilon}_{\mathbf{T,p,m}}) + \mathbb{C}_{\mathbf{ss,m}}(\boldsymbol{\Delta\varepsilon}_{\mathbf{s,m}} - \boldsymbol{\Delta\varepsilon}_{\mathbf{T,s,m}}) = \mathbb{C}_{\mathbf{sp,f}}(\boldsymbol{\Delta\varepsilon}_{\mathbf{p,f}} - \boldsymbol{\Delta\varepsilon}_{\mathbf{T,p,f}}) + \mathbb{C}_{\mathbf{ss,f}}(\boldsymbol{\Delta\varepsilon}_{\mathbf{s,f}} - \boldsymbol{\Delta\varepsilon}_{\mathbf{T,s,f}}) \end{gathered} \tag{56}$$

Using Equation 48 and Equation 51 in Equation 56, the initial prediction yields

$$\boldsymbol{\Delta\varepsilon}_{\mathbf{s,m}}\big|_0 = \mathbb{M} : \Big(\mathbb{C}_{\mathbf{sp,m}}\boldsymbol{\Delta\varepsilon}_{\mathbf{s}} + \phi_f(\mathbb{C}_{\mathbf{sp,f}} - \mathbb{C}_{\mathbf{sp,m}})\boldsymbol{\Delta\varepsilon}_{\mathbf{p}} + \phi_f \boldsymbol{\Delta\sigma}_{\mathbf{T,m}} - \phi_f \boldsymbol{\Delta\sigma}_{\mathbf{T,f}} \Big) \tag{57}$$

$$\mathbb{M} = \Big(\phi_f \mathbb{C}_{\mathbf{ss,m}} + \phi_m \mathbb{C}_{\mathbf{ss,f}} \Big)^{-1} \tag{58}$$

$$\boldsymbol{\Delta\sigma}_{\mathbf{T,m}} = \mathbb{C}_{\mathbf{sp,m}}\boldsymbol{\Delta\varepsilon}_{\mathbf{T,p,m}} + \mathbb{C}_{\mathbf{ss,m}}\boldsymbol{\Delta\varepsilon}_{\mathbf{T,s,m}} \tag{59}$$

$$\boldsymbol{\Delta\sigma}_{\mathbf{T,f}} = \mathbb{C}_{\mathbf{sp,f}}\boldsymbol{\Delta\varepsilon}_{\mathbf{T,p,f}} + \mathbb{C}_{\mathbf{ss,f}}\boldsymbol{\Delta\varepsilon}_{\mathbf{T,s,f}} \tag{60}$$

where $\Delta\,\sigma_{T,f}$ is the fibre incremental thermal stressa nd $\Delta\,\sigma_{T,m}$ is the matrix incremental thermal stress. Both terms are the result of extending the regular SP-RoM in [20] in order to take into account the effect of deformation under elevated temperatures.

The definition in Equation 50 is valid for each of the constituent materials, however the homogenised tangent elastic constitutive tensor can be obtained from the derivation of Equation 48 and Equation 49 ([20])

$$\mathbb{C}_{\mathbf{tan}} := \mathbb{C}_{\mathbf{pp}} + \mathbb{C}_{\mathbf{ps}} + \mathbb{C}_{\mathbf{sp}} + \mathbb{C}_{\mathbf{ss}} \tag{61}$$

where $\mathbb{C}_{\mathbf{pp}}$, $\mathbb{C}_{\mathbf{ps}}$, $\mathbb{C}_{\mathbf{sp}}$ and $\mathbb{C}_{\mathbf{ss}}$ are the parallel-parallel, parallel-serial, serial-parallel and serial-serial tangent elastic constitutive matrices. The expressions of these matrices are described in [20]. The tangent elastic constitutive matrix can be also expressed in in-plane and out-of-plane components using the following relationship

$$\begin{bmatrix} \mathrm{d}\boldsymbol{\sigma}_{\text{in}} \\ \mathrm{d}\boldsymbol{\sigma}_{\text{out}} \end{bmatrix} = \mathbb{C}_{\mathbf{tan}} \begin{bmatrix} \mathrm{d}\boldsymbol{\varepsilon}_{\text{in}} - \mathrm{d}\boldsymbol{\varepsilon}_{\mathbf{T}} \\ \mathrm{d}\boldsymbol{\varepsilon}_{\text{out}} \end{bmatrix} = \begin{bmatrix} \mathbb{C}_{\text{in-in}} & \mathbb{C}_{\text{in-out}} \\ \mathbb{C}_{\text{out-in}} & \mathbb{C}_{\text{out-out}} \end{bmatrix} \begin{bmatrix} \mathrm{d}\boldsymbol{\varepsilon}_{\text{in}} - \mathrm{d}\boldsymbol{\varepsilon}_{\mathbf{T}} \\ \mathrm{d}\boldsymbol{\varepsilon}_{\text{out}} \end{bmatrix} \tag{62}$$

where $\boldsymbol{\sigma}_{\text{in}} := [\sigma_x, \sigma_y, \tau_{xy}]^T$ is the in-plane stress vector, $\boldsymbol{\sigma}_{\text{out}} := [\tau_{yz}, \tau_{zx}]^T$ is the out-of-plane stress vector, $\boldsymbol{\varepsilon}_{\text{in}} := [\varepsilon_x, \varepsilon_y, \gamma_{xy}]^T$ is the in-plane stress vector, $\boldsymbol{\varepsilon}_{\text{out}} := [\gamma_{yz}, \gamma_{zx}]^T$ is the out-of-plane stress vector and $\Big(\boldsymbol{\varepsilon}_{\mathbf{T}} := [\phi_f \alpha_{x,f} + \phi_m \alpha_{x,m}, \phi_f \alpha_{y,f} + \phi_m \alpha_{y,m}, 0]^T \Delta T\Big)$ is the thermal strain.

3.4. Shell finite element

In the thermomechanical coupling, the mechanical model is based on the Reissner-Mindlin flat shell theory ([24], [25]). The four-noded QLLL flat shell quadrilateral element proposed in [30] has been chosen as the finite element solution to model the Reisnner-Mindlin flat shell theory. This shell element combines the classical 4-noded plane stress quadrilateral matrix ([31]) and the QLLL plate element ([32]). The constitutive model for this shell element is the one detailed in section 3.3.

The middle plane of the structure is discretised by 4-node quadrilateral shell elements. The local axis of each quadrilateral element is defiend as (x', y', z') where the vertical local axis (z') is taken normal to the middle plane $(x'y')$ and belong the union of the edges $\left(\overline{12} \cup \overline{14}\right)$ (Figure 1). The thickness of each element is divided in n_{layers} layers. Each layer i lies between the plane $({z_l}')$ and $({z_{l+1}}')$. It is assumed that each layer satisfy the plane stress hypothesis ($\sigma_{z'} = 0$ and the displacements in the directions of the axes (x', y', z') are defined as (u', v', w') respectively.

Taking into account that the strain $(\varepsilon_{z'})$ does not generate work, because of the plane stress assumption, the pertinent strains of the Reissner-Mindlin shell theory are written in local axes as

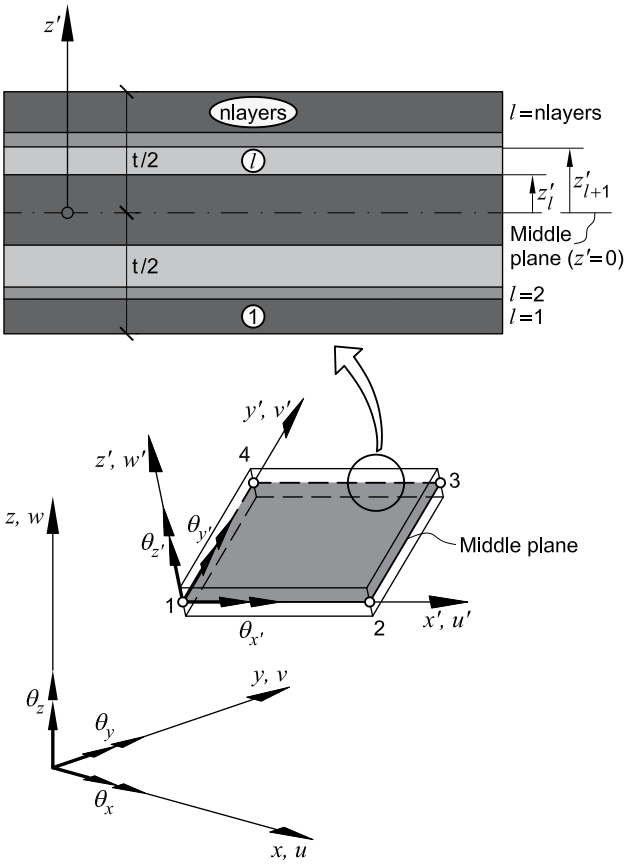

Figure 1: Local and global description of kinematics for the 4-node quadrilateral shell element.

$$\boldsymbol{\varepsilon}' = \begin{bmatrix} \varepsilon_{x'} \\ \varepsilon_{y'} \\ \gamma_{x'y'} \\ \gamma_{x'z'} \\ \gamma_{y'z'} \end{bmatrix} \equiv \begin{bmatrix} \dfrac{\partial u'}{\partial x'} \\ \dfrac{\partial v'}{\partial y'} \\ \dfrac{\partial u'}{\partial y'} + \dfrac{\partial v'}{\partial x'} \\ \dfrac{\partial u'}{\partial z'} + \dfrac{\partial w'}{\partial x'} \\ \dfrac{\partial v'}{\partial z'} + \dfrac{\partial w'}{\partial y'} \end{bmatrix} = \begin{bmatrix} 1 & 0 & 0 & -z' & 0 & 0 & 0 & 0 \\ 0 & 1 & 0 & 0 & -z' & 0 & 0 & 0 \\ 0 & 0 & 1 & 0 & 0 & -z' & 0 & 0 \\ 0 & 0 & 0 & 0 & 0 & 0 & 1 & 0 \\ 0 & 0 & 0 & 0 & 0 & 0 & 0 & 1 \end{bmatrix} \begin{bmatrix} \hat{\boldsymbol{\varepsilon}}_{\mathbf{m}}{}' \\ \hat{\boldsymbol{\varepsilon}}_{\mathbf{b}}{}' \\ \hat{\boldsymbol{\varepsilon}}_{\mathbf{s}}{}' \end{bmatrix} = \mathbf{S}\hat{\boldsymbol{\varepsilon}}' \tag{63}$$

where $\hat{\boldsymbol{\varepsilon}}_{\mathbf{m}}{}'$, $\hat{\boldsymbol{\varepsilon}}_{\mathbf{b}}{}'$ and $\hat{\boldsymbol{\varepsilon}}_{\mathbf{s}}{}'$ are the generalised local strain vectors due to membrane, bending and shear effects respectively (see [30]), $\hat{\boldsymbol{\varepsilon}}'$ is the generalised strain field vector and $\mathbf{S}$ is the linear transformation matrix for strain decoupling.

The discretisation of the generalised strain field $\hat{\boldsymbol{\varepsilon}}'$ presented in this article can be written as

$$\hat{\boldsymbol{\varepsilon}}' = \begin{bmatrix} \mathbf{B1}' & \mathbf{B2}' & \mathbf{B3}' & \mathbf{B4}' \end{bmatrix} \begin{bmatrix} \mathbf{a_1}' \\ \mathbf{a_2}' \\ \mathbf{a_3}' \\ \mathbf{a_4}' \end{bmatrix} = \mathbf{B}'\mathbf{a}' \tag{64}$$

where $\mathbf{Bi}' := \left[\mathbf{Bm, i}', \mathbf{Bb, i}', \mathbf{Bs, i}'\right]^T$ is the displacement-strain matrix for the node i, $\mathbf{Bm, i}'$, $\mathbf{Bb, i}'$ and $\mathbf{Bs, i}'$ are the membrane, bending and shear displacement-strain matrices respectively for the node i. And the local displacements vector for node i is defined as $\mathbf{a_i}' := \left[u_{0,i}{}', v_{0,i}{}', w_{0,i}{}', \theta_{x',i}, \theta_{y',i}\right]^T$. See [30] for further detail on the procedure to obtain the expressions for the membrane, bending and shear nodal displacement-strain matrices.

The generalised stress vector ($\hat{\boldsymbol{\sigma}}'$) at the middle plane of an element can be written as

$$\hat{\boldsymbol{\sigma}}' = \begin{bmatrix} \hat{\boldsymbol{\sigma}}_{\mathbf{m}}{}' \\ \hat{\boldsymbol{\sigma}}_{\mathbf{b}}{}' \\ \hat{\boldsymbol{\sigma}}_{\mathbf{s}}{}' \end{bmatrix} = \sum_{l=1}^{n_{\text{layers}}} \begin{bmatrix} (z_{l+1}{}' - z_l{}')\boldsymbol{\sigma}_{\text{in,l}}{}' \\ \frac{1}{2}({z_{l+1}}'^2 - {z_l}'^2)\boldsymbol{\sigma}_{\text{in,l}}{}' \\ (z_{l+1}{}' - z_l{}')\boldsymbol{\sigma}_{\text{out,l}}{}' \end{bmatrix} \tag{65}$$

where $\hat{\boldsymbol{\sigma}}_{\mathbf{m}}{}' = [N_{x'}, N_{y'}, N_{x'y'}]^T$, $\hat{\boldsymbol{\sigma}}_{\mathbf{b}}{}' = [M_{x'}, M_{y'}, M_{x'y'}]^T$ and $\hat{\boldsymbol{\sigma}}_{\mathbf{s}}{}' = [Q_{x'}, Q_{y'}]^T$ are the resultant stress vector corresponding to membrane, bending and shear effects respectively. $\boldsymbol{\sigma}_{\text{out,l}}{}'$ and $\boldsymbol{\sigma}_{\text{in,l}}{}'$ are the in-plane and transverse stress vectors of the layer l that are defined in Equation 62, however in this case it is expressed in the element local axis.

The residual vector of forces expressed in the local axes can obtained starting from the principle of virtual work and applying the classical procedure in finite element methodology.

$$\mathbf{r_a}{}'_{\Omega_e} = \mathbf{f}_{\text{int}}{}'_{\Omega_e} - \mathbf{f}_{\text{ext}}{}'_{\Omega_e} = \int_{\Omega_e} (\mathbf{B}')^T \hat{\boldsymbol{\sigma}}' \, \mathrm{d}\Omega_e - \int_{\Omega_e} \mathbf{N}^T \hat{\boldsymbol{\tau}}' \, \mathrm{d}\Omega_e \tag{66}$$

where $\mathbf{f}_{\text{int}}{}'_{\Omega_e}$ and $\mathbf{f}_{\text{ext}}{}'_{\Omega_e}$ are the elemental internal and external force vector in local description, and $\mathbf{N}$ is the classic mechanical shape function[31] and $\hat{\boldsymbol{\tau}}' := [q_{x'}, q_{y'}, q_{z'}, m_{x'}, m_{y'}, m_{z'}]$ is the external traction force vector.

In order to transform these magnitudes from local to global axes, it typically is carried out by multiplying by a linear transformation T_{Ω_e} [30]. Then the residual vector of forces in global axes is expressed

$$\mathbf{r}_{\mathbf{a}\Omega_e} = \mathbf{T}^T_{\Omega_e} \mathbf{r_a}{}'_{\Omega_e} = \mathbf{f}_{\text{int}\Omega_e} - \mathbf{f}_{\text{ext}\Omega_e} = \mathbf{T}^T_{\Omega_e} \mathbf{f}_{\text{int}}{}'_{\Omega_e} - \mathbf{T}^T_{\Omega_e} \mathbf{f}_{\text{ext}}{}'_{\Omega_e} \tag{67}$$

where $\mathbf{f}_{\text{int}\Omega_e}$ and $\mathbf{f}_{\text{ext}\Omega_e}$ are the element internal and external force vector in global description. The residual vector of forces of the whole structure is obtained by the assembling of the elements and the equilibrium equations yield

$$\mathbf{r_a}(\mathbf{a}, \mathbf{T}) = \sum_{e=1}^{n_{\text{elem}}} \mathbf{r}_{\mathbf{a}\Omega_e} = \sum_{e=1}^{n_{\text{elem}}} \mathbf{f}_{\text{int}\Omega_e} - \sum_{e=1}^{n_{\text{elem}}} \mathbf{f}_{\text{ext}\Omega_e} = \mathbf{f}_{\text{int}}(\mathbf{a}, \mathbf{T}) - \mathbf{f}_{\text{ext}} = \mathbf{0} \tag{68}$$

where $\mathbf{a}$ is the global displacements vector. Equation 68 represents a non-linear problem due to geometrical and material non-linearities. The solution can be found by the Newton Rapshon method together with the application of an incremental-iterative scheme ([33]). Linearising Equation 68 yields

$$\mathbf{r_a}(\mathbf{a},\mathbf{T})\big|_{n+1,k+1} = \mathbf{r_a}(\mathbf{a},\mathbf{T})\big|_{n+1,k} + \mathbf{K}|_{n+1,k}\ \mathbf{\Delta a}|_{n+1,k+1}\,, \quad \text{with} \quad \mathbf{K}(\mathbf{a},\mathbf{T})|_{n+1,k} = \sum_{e=1}^{n_{\text{elem}}} \left.\frac{\partial \mathbf{r}_{\mathbf{a}\Omega_e}}{\partial \mathbf{a},\mathbf{T}}\right|_{n+1,k} \tag{69}$$

$$\mathbf{\Delta a}|_{n+1,k+1} = -\left.\mathbf{K}^{-1}\right|_{n+1,k} \mathbf{r_a}(\mathbf{a},\mathbf{T})\big|_{n+1,k} \tag{70}$$

where $\left.\mathbf{K}^{-1}\right|_{n+1,k}$ is the global tangent stiffness matrix and $\left.\dfrac{\partial \mathbf{r}_{\mathbf{a}\Omega_e}}{\partial \mathbf{a}}\right|_{n+1,k}$ is calculated using the expression

$$\left.\frac{\partial \mathbf{r}_{\mathbf{a}\Omega_e}}{\partial \mathbf{a}}\right|_{n+1,k} = \mathbf{T}^T_{\Omega_e} \int_{\Omega_e} (\mathbf{B}')^T\ \mathbf{D}'\big|_{n+1,k}\, \mathbf{B}'\, \mathrm{d}\Omega_e \mathbf{T}_{\Omega_e} \tag{71}$$

where $\mathbf{D}'|_{n+1,k}$ is the generalised constitutive matrix. This matrix can be calculated, in terms of the tangent constitutive matrices of each layer defined in Equation 61, as follows

$$\begin{aligned}
\mathbf{D}'\big|_{n+1,k} &:= \left.\begin{bmatrix} \mathbf{D_{mm}}' & \mathbf{D_{mb}}' & \mathbf{D_{ms}}' \\ \mathbf{D_{bm}}' & \mathbf{D_{bb}}' & \mathbf{D_{bs}}' \\ \mathbf{D_{sm}}' & \mathbf{D_{sb}}' & \mathbf{D_{ss}}' \end{bmatrix}\right|_{n+1,k} \\
&= \sum_{l=1}^{n_{\text{layers}}} \left.\begin{bmatrix} (z_{l+1}' - z_l')\mathbb{C}_{\text{in-in,l}} & \frac{1}{2}({z_{l+1}'}^2 - {z_l'}^2)\mathbb{C}_{\text{in-in,l}} & (z_{l+1}' - z_l')\mathbb{C}_{\text{in-out,l}} \\ \frac{1}{2}({z_{l+1}'}^2 - {z_l'}^2)\mathbb{C}_{\text{in-in,l}} & \frac{1}{3}({z_{l+1}'}^3 - {z_l'}^3)\mathbb{C}_{\text{in-in,l}} & \frac{1}{2}({z_{l+1}'}^2 - {z_l'}^2)\mathbb{C}_{\text{in-out,l}} \\ (z_{l+1}' - z_l')\mathbb{C}_{\text{out-in,l}} & \frac{1}{2}({z_{l+1}'}^2 - {z_l'}^2)\mathbb{C}_{\text{out-in,l}} & (z_{l+1}' - z_l')\mathbb{C}_{\text{out-out,l}} \end{bmatrix}\right|_{n+1,k}
\end{aligned} \tag{72}$$

Equation 69 represents a non-linear problem that depends of the state variable (a) and its non-linear constitutive model in Equation 72 depends on the thermal model (T, F). The thermo-mechanical model solution is shown in algorithm 1.

Algorithm 1: Non-linear thermomechanical coupling

$n = 0$ // Initialise;
while $n \leq n_{max}$ **do**
THERMAL PROBLEM;
$k = 0$;
$\mathbf{T}|_{n+1,k} = \mathbf{T}|_n$;
while $k \leq k_{max}$ **do**
$\mathbf{T}|_{n+1,k+1} = \mathbf{T}|_{n+1,k}$;
$\mathbf{L_T}\big|_{n+1,k}\ \mathbf{\Delta T}|_{n+1,k+1} = -\ \mathbf{r_T}\big|_{n+1,k}$ // $\mathbf{L_T}\big|_{n+1,k} = \left.\dfrac{\partial \mathbf{r_T}}{\partial \mathbf{T}}\right|_{n+1,k}$;
$\mathbf{T}|_{n+1,k+1} = \mathbf{T}|_{n+1,k} + \mathbf{\Delta T}|_{n+1,k+1}$ // Update $F|_{n+1,k+1}$;
if $\dfrac{\left|\left|\mathbf{r_T}\big|_{n+1,k}\right|\right|}{\left|\left|\mathbf{q}_{ext}\big|_{n+1,k}\right|\right|} \leq tolerance;$
then
$\mathbf{T}|_{n+1} = \mathbf{T}|_{n+1,k+1}$;
break;
else
$k = k + 1$;
THERMOMECHANICAL PROBLEM;
$k = 0$;
$\mathbf{a}|_{n+1,k} = \mathbf{a}|_n$;
while $k \leq k_{max}$ **do**
$\mathbf{a}|_{n+1,k+1} = \mathbf{a}|_{n+1,k}$;
$\mathbf{K}|_{n+1,k}\ \mathbf{\Delta a}|_{n+1,k+1} = -\ \mathbf{r_a(a,T)}\big|_{n+1,k}$ // $\mathbf{K(a,T)}|_{n+1,k} = \left.\dfrac{\partial \mathbf{r_a(a,T)}}{\partial \mathbf{a}}\right|_{n+1,k}$;
$\mathbf{a}|_{n+1,k+1} = \mathbf{a}|_{n+1,k} + \mathbf{\Delta a}|_{n+1,k+1}$
if $\dfrac{\left|\left|\mathbf{r_a(a,T)}\big|_{n+1,k}\right|\right|}{\left|\left|\mathbf{f}_{ext}\big|_{n+1,k}\right|\right|} \leq tolerance;$
then
$\mathbf{a}|_{n+1} = \mathbf{a}|_{n+1,k+1}$;
break;
else
$k = k + 1$;
$n = n + 1$;

4. Validation of the numerical model

4.1. Henderson experimental tests

In order to validate the thermal part of the thermomechanical model developed in this work, the experimental data presented in Henderson et al. in [3] will be used. In the experimental tests, a composite material consisting of $\phi_m = 39.5\%$ of phenolic resin and $\phi_f = 60.5\%$ of glass and talc filler was studied. The test samples were of cylindrical shape of 1cm diameter by 3cm height. The tests consisted of exposing one side of these samples to a radiant heat flux of 279.7kW/m^2. The temperature evolution of the samples was monitored using four thermocouples at depths of 0.1, 0.5, 1.0 and 2.9cm from the heated side. The instrumentation, sensors and experimental procedure is described in [34].

These experimental tests have been simulated with the numerical model developed in this work. The cylindrical samples have been modelled with 30 finite elements of 1D. The material properties and boundary conditions that have been used in the simulations are the same as those reported in [3].

The Figure 2 shows the time evolution of the temperatures obtained from the experimental test and the numerical model is compared.

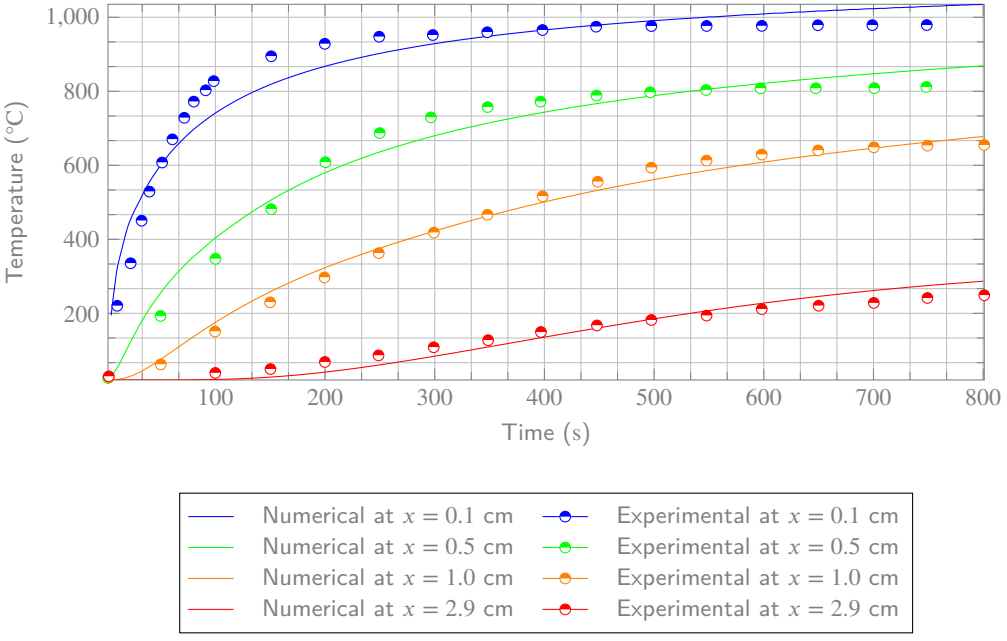

Figure 2: Evolution of the temperature $(T(x,t))$ of the experimental and numerical results at different thickness positions.

It can be observed that the agreement between the numerical and experimental results is excellent.

4.2. Fire-resistant test on a load-bearing bulkhead

The second validation exercise will be done against the experimental test of a FRP bulkhead following the standards of the International Code for Application of Fire Test Procedures (2010 FTP Code) [35, Part 11]. This test has been carried out within the scope of the H2020 Fibreship project in the vertical furnace of Eurofins Expert Services. The test was aimed at demonstrating the performance of the bulkhead as a 60 minutes load bearing fire resistant division. In order to study the performance of the bulkhead beyond those 60 minutes, the test was extended until 5100 s, where it had to be finished due to safety reasons. At that instant, the panel deformation created a significant

gap with the frame allowing the flames to start escaping.

A FRP division was manufactured with the dimensions and characteristics shown in Figure 4. A total of 5 sensors – represented as groups of three squared pattern markers in Figure 4 – are placed at (25%,25%), (75%,25%), (50%,50%), (25%,75%) and (75%,75%) where each coordinate is relative to the width (2.9m) and height (2.98m) of the panel. Each of these groups of sensors are composed of 3 through-thickness thermocouples placed on the unexposed surface, in the middle of the PVC and behind the monolithic laminate bounded to the insulation (see Figure 4).

The experiment was performed as established by the standards([36],[37]), which determines the heat flux based on a design temperature curve. The calibrated heat flux is correct as the furnace temperature matches perfectly the ISO 834 curve . The standard emissivity value of 0.9 is used for both unexposed and exposed surfaces, the standard convection coefficient for the unexposed surface is 9 ($W/m^2°K$) and for the exposed should be 25 ($W/m^2°K$), however the sensitivity tests have shown that its real value is more of the order of 15 ($W/m^2°K$). The temperature, at which the unexposed surface is considered to be the ambient, is 17(°C).

Figure 3: Experimental setup for the bulkhead test.

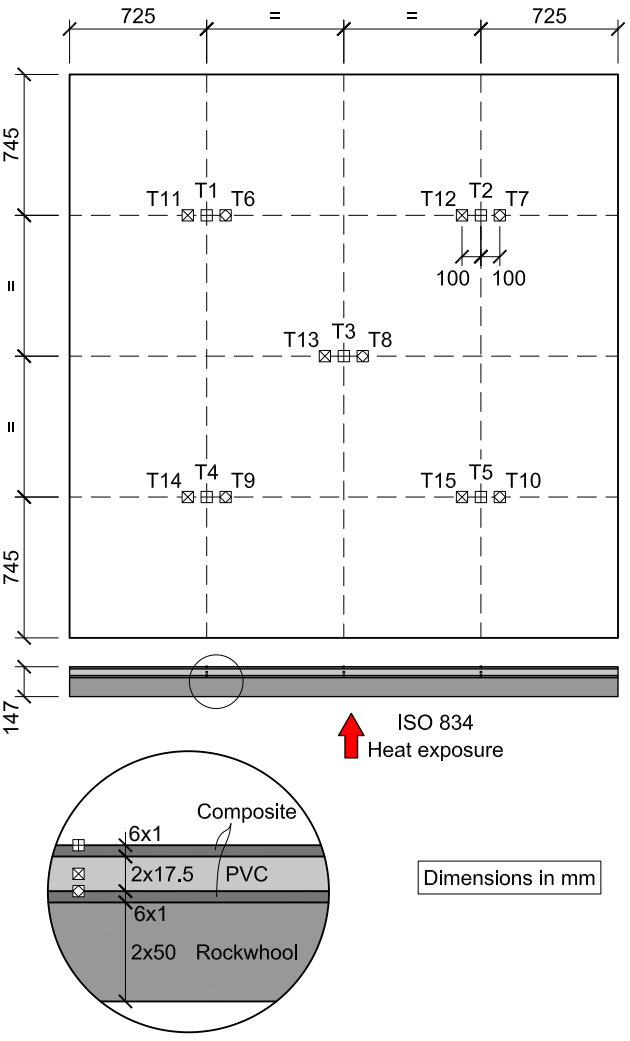

Figure 4: Schematic of the test panel.

The International Maritime Organisation (IMO) in their Fire Test Procedures guidelines[35, Part 11] establish also the mechanical load conditions used in the test. The load condition is a compression load of 7.0 kN/m placed on the top edge.The mechanical deflection in the centre of the panel was measured by an actuated cable sensor and later compared with the numerical results.

The composite laminate is conformed by the following stack where the layup is shown in Figure 4:

Layer 1: 16×0.375mm layers of unidirectional glass/vinylester (LEO Injection Resin 8500 from BÜFA; this resin is part of the Saertex LEO® fire retardant composite system) and the fibre orientation of the stack is [0 90 ,0 ,90 ,0 ,45 ,-45 ,90 ,0 ,90 ,0 ,45 ,-45 ,90 ,0 ,90] degrees [38].

Layer 2: 2×17.5mm layers of PVC which works as the core of the sandwich (PVC-H80 from Diab Group; this

core is part of the Divinycell H® materials) [39].

Layer 3: 16×0.375mm layers of unidirectional glass/vinylester (LEO Injection Resin 8500 from BÜFA; this resin is part of the Saertex LEO® fire retardant composite system) and the fibre orientation of the stack is [90 ,0 ,90 ,-45 ,45 ,0 ,90 ,0 ,90 ,-45 ,45 ,0 ,90 ,0 ,90 ,0] degrees.

Layer 4: 2×50mm layers mineral wool which works as an insulation of the composite laminate material (SeaRox® SL 620 from Rockwool) [40].

The thermal properties of each layer material are presented in Table 1

Material	k (W/m°K)	C_p (J/m^2°K)	C_{p_g} (J/m^2°K)	ρ_s (kg/m^3)	Q_p (J/kg)
glass/vinylester	0.5135	858.55	1000 - 1200	1780	$2{\cdot}10^5$
PVC	0.02-0.06	1170	1200	80	0
rockwool	0.03-0.8	1000-750	0	60	0

Table 1
Calibrated thermal properties of the layer materials.

The decomposition energy of the PVC is neglected, since the temperature measured in the core of the bulkhead throughout the test was lower than the degradation temperature threshold.

The pyrolisis model of the laminate used to build the bulkhead was calibrated against the experimental thermo-gravimetric test which has also been carried out within the context of the Fibreship project. Figure 5a shows the agreement of the mass fraction evolution of the model in the thermo-gravimetric test of the laminate after the calibration. On the other hand, the pyrolisis of the core material of the laminate is taken from the thermo-gravimetric analysis presented in [41] and Figure 5b compares the experimental data from the literature to selected the pyrolisis model for the PVC.

Material	A_T (s^{-1})	E_a (J/kmol)	n_r (J/m^2°K)
glass/vinylester	$6 \cdot 10^{20}$	$2.8{\cdot}10^5$	6
PVC	1202604.28	90000	2

Table 2
Calibrated pyrolisis properties of layer materials.

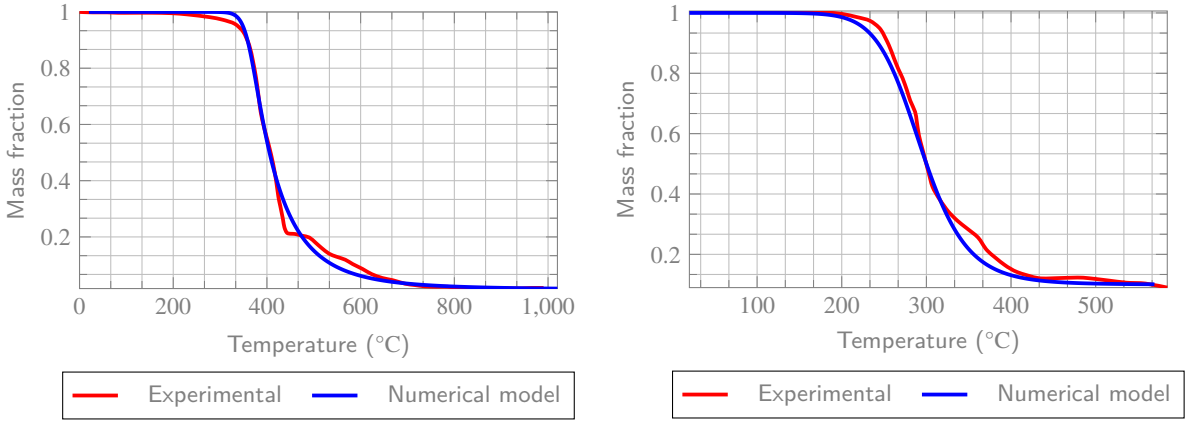

(a) Leo System®.

(b) PVC-H80 [41].

Figure 5: Evolution of the experimental and modelled mass fraction $\left(\frac{\partial \rho_s(T)}{\partial t}\right)$.

The values for the Arrhenius law (Equation 7) of the parameters of the calibrated pyrolysis model in Figure 5a and Figure 5b are given in Table 2. The insulation can be considered pyrolisis free. This means that the degradation factor will remain equal to one and the evolution to zero.

The mechanical properties of the components in the Leo System® material are taken from the experimental data presented in [42]. The PVC is calibrated against the data provided in [39] and any missing information is completed by standard low density PVC values.

Material	E (Pa)	ν	σ_y (MPa)	G_f (N/m)	β	ϕ
Matrix	$3.35 \cdot 10^9$	0.26	20	$1.2 \cdot 10^4$	1	0.40
Fibre	$72.4 \cdot 10^9$	0.21	1800	$8.0 \cdot 10^5$	1	0.60
PVC	$49 \cdot 10^6$	0.4				
rockwool	2466060.9905	$1.17647 \cdot 10^{-6}$				

Table 3
Calibrated mechanical properties of constituent materials [42, 43].

The characterisation of the evolution of the Young modulus respect to the temperature is obtained from a dynamic mechanical thermal analysis (DMTA) of the Leo System® material and for PVC, the storage modulus, is obtained from the research by Earl and Shenoi in [44].

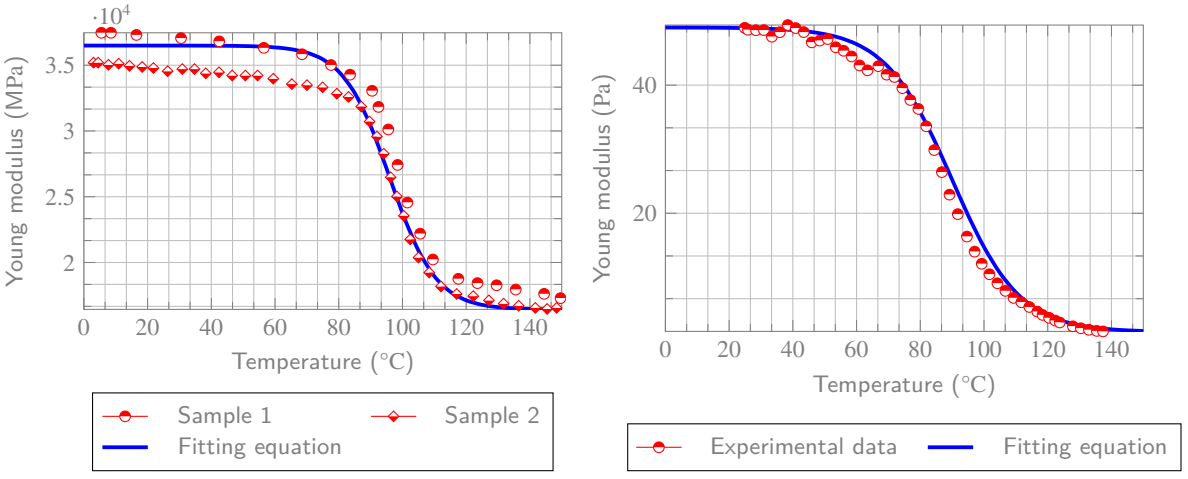

(a) Leo System®.

(b) PVC-H80. (Adapted from [44]).

Figure 6: Experimental and numerical evolution of the storage modulus respect to the temperature.

Material	E_u (MPa)	E_r (MPa)	χ_1	χ_2	T_g (°K)	α (°K^{-1})
Matrix	3350	1507.5	-0.0691	6	96	$36 \cdot 10^{-6}$
Fibre	72400	32580	-0.0691	6	96	$36 \cdot 10^{-6}$
PVC	49	1.47	-0.0475	6	90	$40 \cdot 10^{-6}$
rockwool						$60 \cdot 10^{-6}$

Table 4
Calibrated thermomechanical properties of the constituent materials.

Note that in Table 4, the insulation only takes into account the thermal expansion coefficient which is considered isotropic. The fitting equation in Figure 6 represents the evolution of the Young modulus described in Equation 42 and with the assumptions in Equation 43, Equation 44 and Equation 45. The glass transition temperature or the thermal

expansion coefficient are assumed to be identical for matrix and fibre since the experimental data is referred to the composite material, therefore the properties of the composite are ingrained into its constituent materials for simplicity.

4.2.1. Results of the fire-resistant test on the bulkhead

This section presents the results of the fire-resistant test on the bulkhead and compares them with those of the computational model. Figure 7 compares the time evolution of the temperatures obtained from the experimental test and the numerical model.

The thermal numerical model consists on a discretisation of the thickness of the composite with a total of 112 1D finite elements. The glass/vinyl-ester layers are discretised with 16 uniform spaced elements each, the PVC core is discretised with 20 uniform spaced elements and the insulation with a total of 60 uniform spaced elements.

The temperature of the furnace is prescribed on the exposed surface using the ISO 834 curve and the ambient temperature prescribed in the unexposed surface is considered to be initially at 17 °C and by the end of the experimental test it is near 25 °C. Note that these two temperatures do not refer to the temperature in the exposed/unexposed surfaces themselves, but rather to the nearby temperatures to these surfaces. Hence, the flux can be calculated as established in Equation 21 and Equation 22 and the convection coefficient and emissivity of both surfaces were described in the setup of the experiment in subsection 4.2.

The thermomechanical model consists on a total of 256 equally distributed linear geometric quadrilateral elements with a non-linear constitutive model. From Figure 4 and defining the horizontal axis as x, the vertical axis as y and the out-of-plane axis as z. The lower horizontal edge fixes the translation degrees of freedom in x, y, z, the upper horizontal edge fixes the translation degree of freedom z and has a load applied of 7 $\mathrm{kN/m}$ as described in subsection 4.2.

Both left and right vertical edges fix the translation degree of freedom in z and have a dynamic variable elastic constraint. These two elastic constraints are symmetric and are controlled by the horizontal dilatation of the edges. There are two stages, first the translation degree of freedom in x is given a certain rigidity to simulate the friction of the panel and the frame and later the translation degree of freedom in x is fixed completely. The plausible phenomenon that is addressed in this example is that the panel is able to slide in the test frame, meaning there is a little space reserved and it is occupied as the bulkhead starts dilating due to the increase of temperature. The first stage blocks gradually the movement in x and in the second stage considers that there is no extra space and the boundary condition has become fully fixed.

Both thermal and thermomechanical analysis are solved incrementally with a total simulation time of 5100 s in intervals of 100 s.

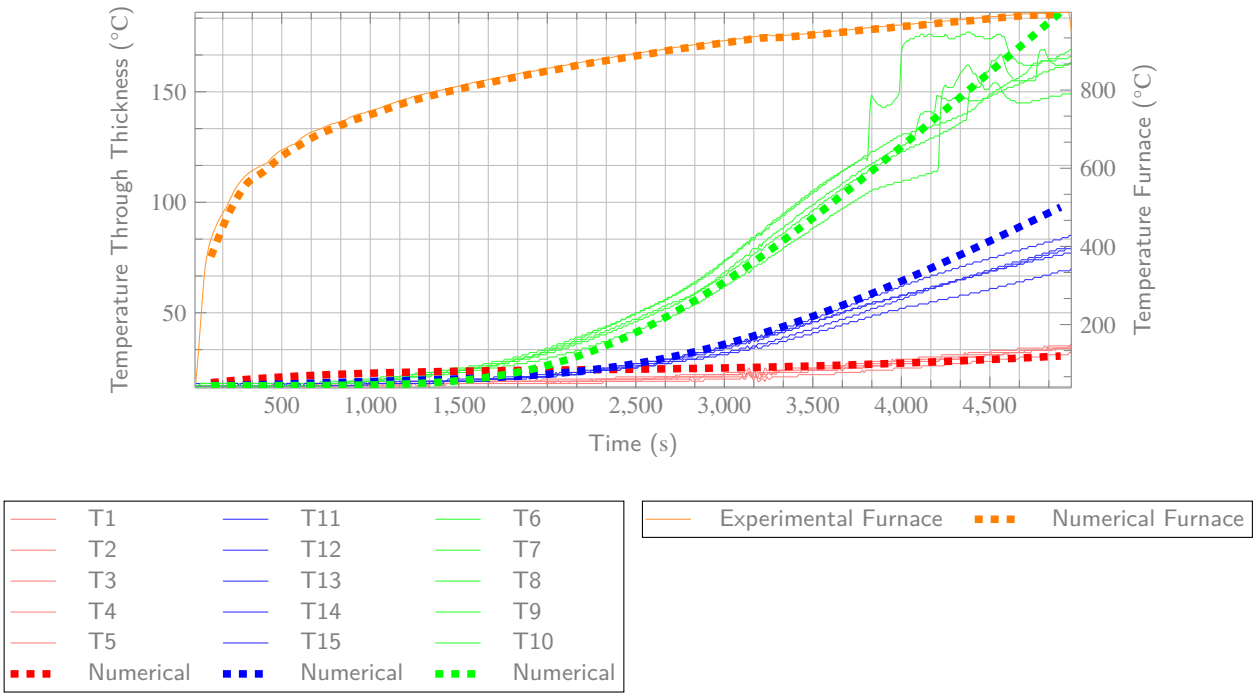

Figure 7: Evolution of the temperature ($T(x,t)$) at different positions of the thickness. The temperature through thickness represents the sets in red, blue and green and the temperature furnace the orange set. Thermocouples T1, T2, T3, T4 and T5 in red were placed at $x = 0.0$ mm, thermocouples T11, T12, T13, T14 and T15 in blue were placed at $x = 25.5$ mm and thermocouples T6, T7, T8, T9 and T10 in green were placed at $x = 41.0$ mm. All measures are respect to the unexposed surface.

Note that both the experimental and computational data closely agree. There is a minor fluctuation of the temperature (green) at the interface between the glass/vinyl-ester layer and the core, closest to the fire exposed surface. This fluctuation is produced near the time the upper right corner of the panel starts to bulge outwards producing a gap between the specimen and the test frame, these the two thermocouples, which have registered these fluctuations, coincide exactly with those that are situated in the upper right and upper left of the panel.

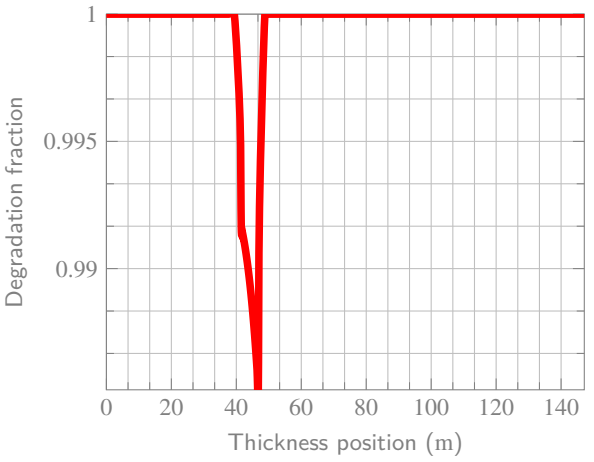

(a) Sectional degradation fraction (F) at time 5100s.

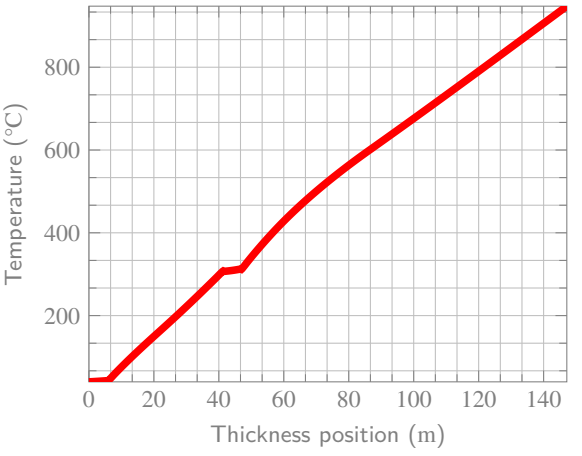

(b) Sectional temperature (T) at time 5100s.

Figure 8: Computed final profile of the degradation and temperature through thickness of the section in the mid point of the panel.

The profile of the degradation fraction at 5100s, computed by the pyrolisis model at the mid point of the panel, is presented in Figure 8a. Notice that the degradation can be considered zero since the minimum degradation fraction is 0.985. It implies that the fire-resistant performance of the panel is excellent.

The corresponding profile of the temperature can be found in Figure 8b, agreeing that the the composite is well insulated. The 4 layers of the composite described previously can be observed by checking the slope variation. Within those 4 regions, only two regions show a temperature over the range of 200 °C.

The degradation shown is in accordance to what was presented in Figure 5a. Notice that the mass fraction presents a substantial change for temperatures higher than 300−400 °C and this is the primary reason why the Leo System® closest to the exposed surface does not present a significant degradation. Similarly, Figure 5b shows that the mass fraction of the PVC starts degrading for temperatures above 200 °C and the PVC region almost reaches this temperature in the union with the Leo System® layer closest to the exposed surface.

The deflection in the middle of the panel is measured with a cable actuated sensor.

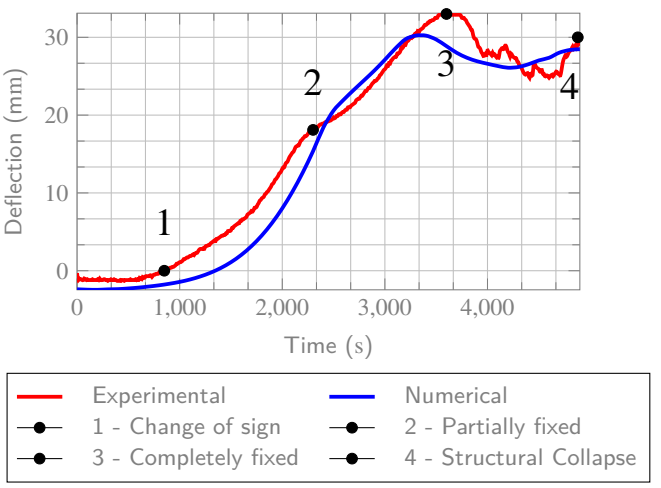

Figure 9: Deflection evolution in mm.

In Figure 9 the deflection in the mid point of the unexposed surface is registered experimentally and compared to the numerical simulation. A good global agreement between computed and measured data is found. However, relevant differences are found in some phases of the test, likely due to the complexity of the problem and the uncertainties in some material properties. This is discussed below.

Throughout the experiment, we can identify four phases, defined by the points 1, 2, 3 and 4 in Figure 9. The panel start deflecting negatively due to the compression load that the panel has to endure according to [35]. Note from Figure 4, the section is non-isotropic and hence the load that is theoretically placed in the middle of the thickness which does not coincide with the neutral axis of the section. This generates two moments in the upper and lower edges each bending the structure, in addition, since the elastic modulus of the section is lower in the insulation than in the glass/vinyl-ester layer, the composite initially experiments a higher compression on the exposed surface (insulation). Thus, the exposed surface is relatively compressed and the unexposed is relatively tensed. The numerical simulation does not fit exactly the early deflection, however it captures the phenomenology, starting with a negative deflection and once the temperature is high enough, it bends to the opposite direction (point 1).

Since the panel is inserted into the test frame, which means it is not fixed in any other direction other than the out-of-plane direction, and the increase of temperature makes the panel to proportionally dilate. It happens around the time step of point 2, in Figure 9, that the specimen edges have started to partially contact the frame and to be fixed to it. In order to model this phenomenon, two boundary conditions – namely two dynamic elastic constraints – were introduced on both vertical edges (right and left) which add an extra fixation on the horizontal direction opposite to the dilatation of the panel. As shown from point 2 onward, this dynamic elastic constraints is able to reproduce the friction condition between the bulkhead and the test frame.

Once the simulation arrives to point 3, the panel is fully fixed due to experimenting an elevated temperature and the fact that there is no reserved extra space to dilate. The dynamic boundary conditions from the third point onward fix the in-plane horizontal translation.

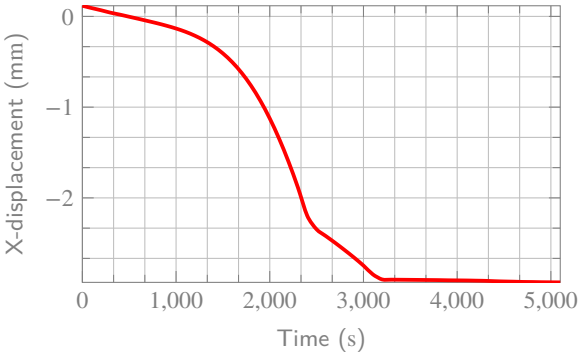

(a) Left mid point.

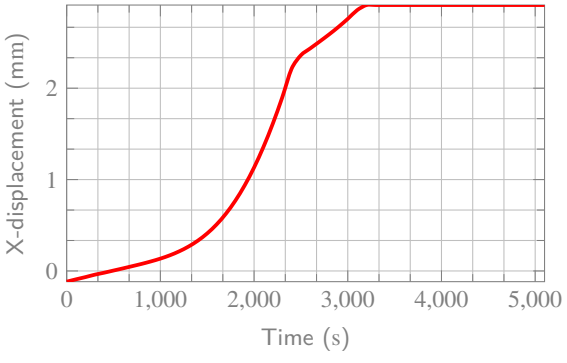

(b) Right mid point.

Figure 10: Horizontal displacement in terms of time. Note the dynamic boundary condition stages.

The numerical model is able to reproduce the behaviour of the third stage to a certain extend, note that the uncertainties and limitations of the experimental test play a fundamental role in this stage. The panel approaching point 4 starts to present a non-symmetrical behaviour and finally the panel collapses when the upper right corner bulges from the test frame. At the fourth point the structure collapses due to the augment of effective mechanical load, since the upper right corner is no longer enduring any load.

The collapse could be reproduced, since the non-symmetric behaviour is very complex to be incorporated in this example. It is not even likely to happen in a real bulkhead fire collapse scenario. However the bulging can be explain through the deflection of a sectional cut passing through the mid point of the panel (Figure 11a) and the maximum damage index (Figure 11b).

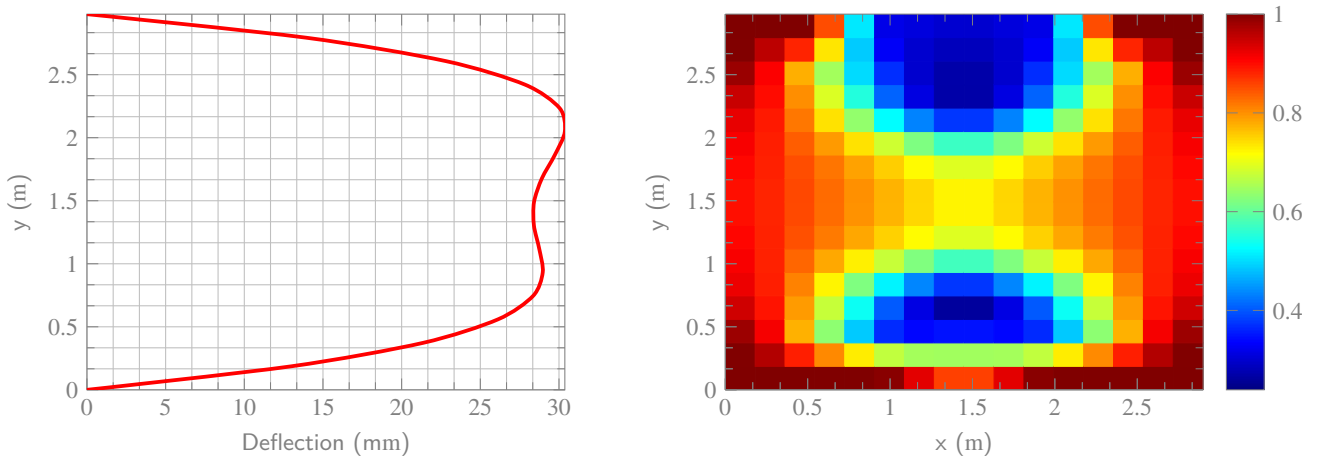

(a) Symmetric vertical section.

(b) Damage index (d).

Figure 11: Final snapshot of the panel at time 5100 s before the experimental test collapses. Observe the damage localisation

In Figure 11 it can be seen that the deflection of the panel presents two protuberances. This is equivalent to the two blue regions found in Figure 11b, observe that the lower end of the section cut presents a mild stepper rotation than the upper end, this explains why the bulging occurs on the top rather than on the bottom. The bulging is considered to occur due to uncertainties that cannot be controlled, however the methodology used in this thermomechanical analysis shows that this phenomenon is feasible to occur since the degradation has a double triangle shape which localises the damage in all four corners, however – numerically speaking – it is still able to conserve the perfect contact between the frame and the specimen.

The experimental test has some certain limitations when it comes to maintaining a perfect contact between the bulkhead and the test frame. Once the upper right corner bulges, fire security protocol, establishes to cease the testing. However it is quite interesting to extend the simulation beyond the scope of 5100 seconds and see that the bulging phenomenon can be addressed in the model. Not the phenomenon *per se*, but the prelude to it. Short after the experimental model collapses, the numerical model shows a good agreement with this bulging behaviour since around all four corners a negative deflection starts to form and this very change of the deflection explains the sudden bulge of one of the corners.

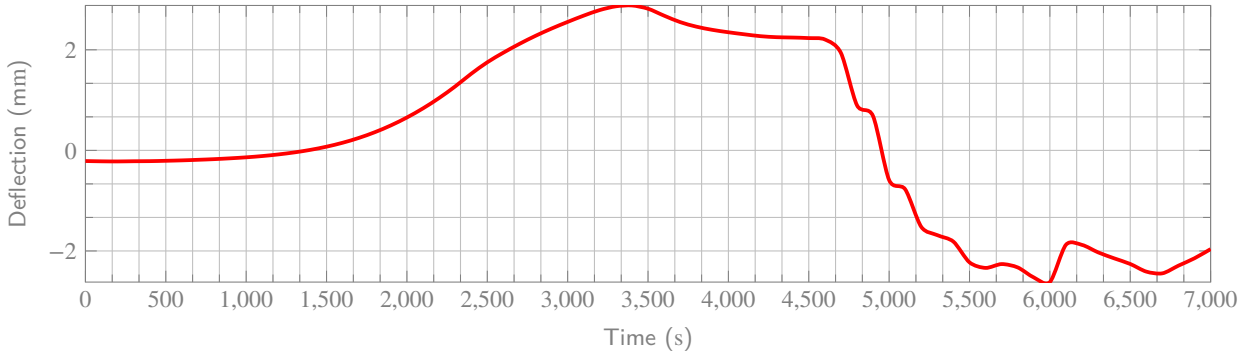

Figure 12: Deflection close to the upper right corner.

Figure 12 shows the evolution of the deflection in the closest node to the corner and does not belong to any of the edges. This node is inside the domain and has no boundary condition applied of any kind. Notice how just close to time 5000s

it bulges outwards of the test frame. The rest of the analysis contemplates a scenario that has not been capable to test in the experiment, however the numerical model assesses the bulging of the node closest to the right upper corner and maintains it for the rest of the extended simulation time. So this clearly shows that the bulging phenomenon – which is the sole reason for the collapse, since the effective section of the bulkhead is reduced considerably – is product of the inability to perfectly retain the edges fixed to the test frame and that the thermomechanical model allows to extend the empirical testing to the hypothetical real scenario.

5. Conclusion

The numerical model detailed in the present work has shown an excellent agreement between the predicted results and the thermal experimental tests as shown firstly in the experimental data provided in [3] (see Figure 2) and also the bulkhead test.

The results from these original experimental tests are almost identical to the numerical results shown in Figure 7, where the numerical model predicts correctly the temperatures registered at different positions of the thickness.

The thermomechanical model, despite not agreeing perfectly, is able to capture the overall behaviour. Note the difficulty to carry out a controlled experiment when fire is involved. The specimen contour is one of the most difficult problems to control (variable boundary conditions) or the fact that little imperfections in the material or mechanical load may result in a non-symmetrical collapse of the structure. Even the instrumentation itself may be limiting to properly register the real deflection.

Eventhough, the thermomechanical analysis shown in Figure 9 is able to assess the structural integrity of the specimen and despite not reproducing the exact collapse phenomenon (non-symmetrical upper right bulging), it has shown to be an excellent tool to perform a fire collapse assessment for composite materials which indeed is one of the novel and unique goals framed in the FibreShip project. The combination of the present pyrolisis model with the simplicity of the SPROM formulation, adapted to high temperatures, grants a unique tool to incorporate the thermal deformation in composites and note the simplicity of using isotropic constituent materials instead of the common and general orthotropic approach.

The importance of using isotropic constituent materials does not reside uniquely on the linear constitutive model, but in the non-linear constitutive model, namely the isotropic damage model, which is a common and standard constitutive model for FRP composite materials. This proposed model is able to introduce the effects of thermal degradation in the non-linear constitutive model and poses a framework to analyse the non-linear structural integrity of composite marine structures as shown in Figure 8. Also the thermomechanical coupling is suitable to analyse different hypothetical fire scenarios when experimental data is missing or limited.

Finally, the original case presented in this work has not addressed the buckling phenomenology, which seemed not to be present in the observed experimental data.

6. Acknowledgement

This work was funded thanks to H2020 project FIBRESHIP sponsored by the EUROPEAN COMMISSION under the grant agreement 723360 "Engineering, production and life-cycle management for complete construction of large-length FIBRE-based SHIPs". www.fibreship.eu/about

7. Disclosure statement

No potential conflict of interest was reported by the authors.

Nomenclature

Notation

P	scalar or tensor notation
$\mathbf{P}$	vector or matrix notation

General

ρ	density $\left(\frac{\mathrm{kg}}{\mathrm{m}^3}\right)$
$\mathbf{L_T}$	left-hand-side temperature matrix $\left(\frac{\mathrm{W}}{\mathrm{m}^3}\right)$
$\mathbf{n}$	normal $\left(\mathrm{m}\right)$
N	shape function
ξ	test function
l_t	thickness $\left(\mathrm{m}\right)$
v	velocity $\left(\frac{\mathrm{m}}{\mathrm{s}}\right)$
ϕ	volume fraction
Ω	domain

Thermal

E_a	activation energy for decomposition reaction of polymer matrix $\left(\frac{\mathrm{J}}{\mathrm{kmol}}\right)$
k	through-thickness thermal conductivity $\left(\frac{\mathrm{W}}{\mathrm{m°C}}\right)$
$\mathbf{K_T}$	conductivity matrix $\left(\frac{\mathrm{W}}{\mathrm{m}^3}\right)$
h_{conv}	convection coefficient
F	degradation fraction
ϵ	emissivity
h	specific enthalpy $\left(\frac{\mathrm{J}}{\mathrm{kg}}\right)$
$\mathbf{q}$	heat flux vector $\left(\frac{\mathrm{W}}{\mathrm{m}^2}\right)$
$\mathbf{B_T}$	gradient matrix $\left(\mathrm{m}^{-1}\right)$
q	heat flux $\left(\frac{\mathrm{W}}{\mathrm{m}^2}\right)$
w	mass flux $\left(\frac{\mathrm{kg}}{\mathrm{m}^2\mathrm{s}}\right)$
$\dot{m}_{s\rightarrow g}$	mass flux rate $\left(\frac{\mathrm{kg}}{\mathrm{m}^2\mathrm{s}}\right)$
A_T	pre-exponential factor for decomposition reaction of polymer matrix $\left(\mathrm{s}^{-1}\right)$
n_r	order of the decomposition reaction of the polymer matrix
$\mathbf{r_T}$	residual heat flux vector $\left(\frac{\mathrm{W}}{\mathrm{m}^2}\right)$
Q	energy source $\left(\frac{\mathrm{J}}{\mathrm{kg}}\right)$
C_p	specific heat capacity $\left(\frac{\mathrm{J}}{\mathrm{kg°C}}\right)$
$\mathbf{C_T}$	specific heat matrix $\left(\frac{\mathrm{W}}{\mathrm{m}^3}\right)$
σ_β	Stefan-Boltzmann constant $\left(5.67 \cdot 10^{-8} \frac{\mathrm{W}}{\mathrm{m}^2 °\mathrm{K}^4}\right)$
T	temperature $\left(°\mathrm{K}\right)$
$\bar{T}$	prescribed temperature $\left(°\mathrm{K}\right)$
R	universal gas constant $\left(8.314 \frac{\mathrm{J}}{\mathrm{kmol}°\mathrm{K}}\right)$

Mechanical

θ	fibre orientation $\left(\mathrm{m}^{-1}\right)$
l_c	characteristic length $\left(\mathrm{m}\right)$
β	compress-traction coefficient
D	constitutive tensor $\left(\mathrm{Pa}\right)$
δ	damage threshold
a	displacement $\left(\mathrm{m}\right)$
$\mathbf{B}$	strain matrix $\left(\mathrm{m}^{-1}\right)$
$\bar{\sigma}$	effective stress $\left(\mathrm{Pa}\right)$
$\mathbb{C}$	elastic constitutive tensor $\left(\mathrm{Pa}\right)$
$\mathbf{f}$	force vector $\left(\mathrm{N}\right)$
G_f	fracture energy $\left(\frac{\mathrm{J}}{\mathrm{m}^2}\right)$
r	normalised internal variable
d	isotropic damage index
ν	Poisson ratio
A	pre-exponential factor of the isotropic damage model
$\mathbf{r_a}$	residual force vector $\left(\mathrm{N}\right)$
$\mathbf{K}$	stiffness matrix $\left(\frac{\mathrm{N}}{\mathrm{m}}\right)$
ε	strain
γ	engineering shear strain
σ	stress $\left(\mathrm{Pa}\right)$
τ	engineering shear stress $\left(\mathrm{Pa}\right)$

ς	stress weight factor	χ	Mourtiz and Gibson fitting parameter
E	Young modulus $\left(\mathrm{Pa}\right)$		
Thermomechanical		α	thermal expansion coefficient $\left(^{\circ}\mathrm{K}^{-1}\right)$

References

[1] A. G. Gibson, P. N. H. Wright, Y. S. Wu, A. P. Mouritz, Z. Mathys, and C. P. Gardiner. The Integrity of Polymer Composites during and after Fire. *Journal of Composite Materials*, 38(15):1283–1307, 8 2004. ISSN 0021-9983. doi: 10.1177/0021998304042733. URL http://journals.sagepub.com/doi/10.1177/0021998304042733.

[2] A. P. Mouritz, S. Feih, E. Kandare, Z. Mathys, A. G. Gibson, P. E. Des Jardin, S. W. Case, and B. Y. Lattimer. Review of fire structural modelling of polymer composites. *Composites Part A: Applied Science and Manufacturing*, 40(12):1800–1814, 2009. ISSN 1359835X. doi: 10.1016/j.compositesa.2009.09.001. URL http://dx.doi.org/10.1016/j.compositesa.2009.09.001.

[3] J.B. Henderson, J.A. Wiebelt, and M.R. Tant. A Model for the Thermal Response of Polymer Composite Materials with Experimental Verification. *Journal of Composite Materials*, 19(6):579–595, 11 1985. ISSN 0021-9983. doi: 10.1177/002199838501900608. URL http://journals.sagepub.com/doi/10.1177/002199838501900608.

[4] J.B. Henderson and T.E. Wiecek. A Mathematical Model to Predict the Thermal Response of Decomposing, Expanding Polymer Composites. *Journal of Composite Materials*, 21(4):373–393, 4 1987. ISSN 0021-9983. doi: 10.1177/002199838702100406. URL http://journals.sagepub.com/doi/10.1177/002199838702100406.

[5] A. G. Gibson, Y. S. Wu, H. W. Chandler, J. A. D. Wilcox, and P. Bettess. A Model for the Thermal Performance of Thick Composite Laminates in Hydrocarbon Fires. *Revue de l'Institut Français du Pétrole*, 50(1):69–74, 1 1995. ISSN 0020-2274. doi: 10.2516/ogst:1995007. URL http://ogst.ifpenergiesnouvelles.fr/10.2516/ogst:1995007.

[6] M. R.E. Looyeh and P. Bettess. A finite element model for the fire-performance of GRP panels including variable thermal properties. *Finite Elements in Analysis and Design*, 30(4):313–324, 10 1998. ISSN 0168874X. doi: 10.1016/S0168-874X(98)00036-5.

[7] N. Dodds, A. G. Gibson, D. Dewhurst, and J. M. Davies. Fire behaviour of composite laminates. *Composites Part A: Applied Science and Manufacturing*, 31(7):689–702, 7 2000. ISSN 1359835X. doi: 10.1016/S1359-835X(00)00015-4.

[8] James Lua, Jeff O'Brien, Christopher T. Key, Yongshu Wu, and Brian Y. Lattimer. A temperature and mass dependent thermal model for fire response prediction of marine composites. *Composites Part A: Applied Science and Manufacturing*, 37(7):1024–1039, 7 2006. ISSN 1359835X. doi: 10.1016/j.compositesa.2005.01.034.

[9] R. D. Chippendale, I. O. Golosnoy, and P. L. Lewin. Numerical modelling of thermal decomposition processes and associated damage in carbon fibre composites. *Journal of Physics D: Applied Physics*, 47(38):385301, 9 2014. ISSN 13616463. doi: 10.1088/0022-3727/47/38/385301. URL http://stacks.iop.org/0022-3727/47/i=38/a=385301http://stacks.iop.org/0022-3727/47/i=38/a=385301?key=crossref.e8e3fa511892bfff723543822db41f64.

[10] A. P. Mouritz and Z. Mathys. Mechanical properties of firedamaged glassreinforced phenolic composites. *Fire and Materials*, 24(2):67–75, 3 2000. ISSN 1099-1018. doi: 10.1002/1099-1018(200003/04)24:2<67::AID-FAM720>3.0.CO;2-0.

[11] A. P. Mouritz and Z. Mathys. Post-fire mechanical properties of marine polymer composites. In *Composite Structures*, volume 47, pages 643–653. Elsevier Science Ltd, 12 1999. doi: 10.1016/S0263-8223(00)00043-X.

[12] A. P. Mouritz and Z. Mathys. Post-fire mechanical properties of glass-reinforced polyester composites. *Composites Science and Technology*, 61(4):475–490, 3 2001. ISSN 02663538. doi: 10.1016/S0266-3538(00)00204-9.

[13] S. Feih, Z. Mathys, A. G. Gibson, and A. P. Mouritz. Modelling the compression strength of polymer laminates in fire. *Composites Part A: Applied Science and Manufacturing*, 38(11):2354–2365, 11 2007. doi: 10.1016/j.compositesa.2007.04.013.

[14] Thomas Keller, Craig Tracy, and Aixi Zhou. Structural response of liquid-cooled GFRP slabs subjected to fire - Part II: Thermo-chemical and thermo-mechanical modeling. *Composites Part A: Applied Science and Manufacturing*, 37(9):1296–1308, 9 2006. ISSN 1359835X. doi: 10.1016/j.compositesa.2005.08.007.

[15] Yu Bai and Thomas Keller. Modeling of mechanical response of FRP composites in fire. *Composites Part A: Applied Science and Manufacturing*, 40(6-7):731–738, 7 2009. ISSN 1359835X. doi: 10.1016/j.compositesa.2009.03.003.

[16] Lingfeng Zhang, Weiqing Liu, Guoqing Sun, Lu Wang, and Lingzhi Li. Two-Dimensional Modeling of Thermomechanical Responses of Rectangular GFRP Profiles Exposed to Fire. *Advances in Materials Science and Engineering*, 2017, 2017. ISSN 16878442. doi: 10.1155/2017/1705915.

[17] Shengbo Shi, Linjie Li, Guodong Fang, Jun Liang, Fajun Yi, and Guochang Lin. Three-dimensional modeling and experimental validation of thermomechanical response of FRP composites exposed to one-sided heat flux. *Materials and Design*, 99:565–573, 6 2016. ISSN 18734197. doi: 10.1016/j.matdes.2016.03.098.

[18] A. E. Green and P. M. Naghdi. A Dynamical theory of interacting continua. *International Journal of Engineering Science*, 3(2):231–241, 7 1965. ISSN 00207225. doi: 10.1016/0020-7225(65)90046-7.

[19] E. Car, S. Oller, and E. Oñate. An anisotropic elastoplastic constitutive model for large strain analysis of fiber reinforced composite materials. *Computer Methods in Applied Mechanics and Engineering*, 185(2-4):245–277, 5 2000. ISSN 00457825. doi: 10.1016/S0045-7825(99)00262-5.

[20] Fernando Rastellini, Sergio Oller, Omar Salomón, and Eugenio Oñate. Composite materials non-linear modelling for long fibre-reinforced laminates. *Computers & Structures*, 86(9):879–896, 5 2008. ISSN 00457949. doi: 10.1016/j.compstruc.2007.04.009. URL https://linkinghub.elsevier.com/retrieve/pii/S0045794907001642.

[21] J. B. Henderson and T. E. Wiecek. A Mathematical Model to Predict the Thermal Response of Decomposing, Expanding Polymer Composites. *Journal of Composite Materials*, 1987. ISSN 1530793x. doi: 10.1177/002199838702100406.

[22] Swedish National Wickstrom Ulf, Dat Duthinh, and Kevin Mcgrattan. Adiabatic Surface Temperature for Calcu-

lating Heat Transfer To Fire Introduction. *Most*, 2, 9 2007. URL https://www.nist.gov/publications/adiabatic-surface-temperature-calculating-heat-transfer-fire-exposed-structures.

[23] Olivier Coussy. *Poromechanics*. John Wiley & Sons, Ltd, Chichester, UK, 12 2003. ISBN 9780470092712. doi: 10.1002/0470092718. URL http://doi.wiley.com/10.1002/0470092718.

[24] E. Reissner. The effect of transverse shear deformation on the bending of elastic plates. *J. Appl. Mech.*, pages A69–A77, 1945.

[25] R. D. Mindlin. Influence of Rotatory Inertia and Shear on Flexural Motions of Isotropic, Elastic Plates. In *The Collected Papers of Raymond D. Mindlin Volume I*, pages 225–232. Springer New York, 1989. doi: 10.1007/978-1-4613-8865-4{_}29.

[26] Eduardo W. V. Chaves. *Notes on Continuum Mechanics*. Lecture Notes on Numerical Methods in Engineering and Sciences. Springer Netherlands, Dordrecht, 2013. ISBN 978-94-007-5985-5. doi: 10.1007/978-94-007-5986-2. URL http://link.springer.com/10.1007/978-94-007-5986-2.

[27] R. Faria, J. Oliver, and M. Cervera. A strain-based plastic viscous-damage model for massive concrete structures. *International Journal of Solids and Structures*, 35(14):1533–1558, 1998. ISSN 00207683. doi: 10.1016/S0020-7683(97)00119-4. URL http://www.sciencedirect.com/science/article/pii/S0020768397001194.

[28] J. Oliver. A consistent characteristic length for smeared cracking models. *International Journal for Numerical Methods in Engineering*, 28 (2):461–474, 2 1989. ISSN 10970207. doi: 10.1002/nme.1620280214. URL http://doi.wiley.com/10.1002/nme.1620280214.

[29] A P Mouritz and A G Gibson. *Fire Properties of Polymer Composite Materials*, volume 143 of *Solid Mechanics and Its Applications*. Springer Netherlands, Dordrecht, 2006. ISBN 978-1-4020-5355-9. doi: 10.1007/978-1-4020-5356-6. URL http://link.springer.com/10.1007/978-1-4020-5356-6.

[30] Eugenio Oñate. Structural Analysis with the Finite Element Method Linear Statics Volume 2. Beams, Plates and Shells. In *Springer*, volume First Edit, chapter 11, pages 675–728. 2013. ISBN 9781402087325. doi: 10.1007/978-1-4020-8743-1. URL http://medcontent.metapress.com/index/A65RM03P4874243N.pdf.

[31] G. R. Liu and S. S. Quek. *The Finite Element Method: A Practical Course: Second Edition*. Elsevier Ltd., 2013. ISBN 9780080983561. doi: 10.1016/C2012-0-00779-X.

[32] Eugenio Oñate. A review of some finite element families for thick and thin plate and shell analysis. 1 1994.

[33] Murray J. Clarke and Gregory J. Hancock. A study of incremental-iterative strategies for non-linear analyses. *International Journal for Numerical Methods in Engineering*, 29(7):1365–1391, 5 1990. ISSN 0029-5981. doi: 10.1002/nme.1620290702. URL http://doi.wiley.com/10.1002/nme.1620290702.

[34] J. B. Henderson and S. C. Hagen. A radiant heat flux apparatus for measuring the thermal response of polymeric materials to high temperatures. *Polymer Composites*, 6(2):110–114, 4 1985. ISSN 0272-8397. doi: 10.1002/pc.750060209. URL http://doi.wiley.com/10.1002/pc.750060209.

[35] International Maritime Organization. *FTP Code : International code for application of fire test procedures, 2010.* International Maritime Organization, 2012. ISBN 9789280115482.

[36] ISO834:1. ISO - ISO 834-11:2014 - Fire resistance tests Elements of building construction Part 11: Specific requirements for the assessment of fire protection to structural steel elements, 3 2014. URL https://www.iso.org/standard/57595.html.

[37] ISO834:2. ISO - ISO 834-2:2019 - Fire-resistance tests Elements of building construction Part 2: Requirements and recommendations for measuring furnace exposure on test samples, 5 2019. URL https://www.iso.org/standard/75137.html.

[38] SAERTEX LEO® Serie. URL https://www.saertex.com/en/products/saertex-leo-serie.

[39] Divinycell H. URL http://www.diabgroup.com/en-GB/Products-and-services/Core-Material/Divinycell-H.

[40] Rockwool Technical Insulation - NEW Improved SeaRox SL 620. URL https://rti.rockwool.com/products/marine-and-offshore/firesafe-insulation/new-improved-searox-sl-620/?selectedCat=marine%20%20offshore%20global.

[41] Barbara Świerz-Motysia and Krzysztof Pielichowski. Kinetics of decomposition of poly(vinyl chloride)/low-migration polyesterarethane plasticizer blend - A thermogravimetric study. In *Polimery/Polymers*, volume 50, pages 601–604, 2005. doi: 10.14314/polimery.2005.601.

[42] Joel Jurado Granados, Xavier Martinez, Niamh Nash, Carlos Bachour, Ioannis Manolakis, Anthony Comer, and Daniel Di Capua. Numerical and experimental procedure for material calibration using the serial/parallel mixing theory, to analyze different composite failure modes. *Mechanics of Advanced Materials and Structures*, 2019. ISSN 15376532. doi: 10.1080/15376494.2019.1675106.

[43] Lucie Chapelle. Characterization and modelling of the mechanical properties of mineral wool. Technical report, 2016.

[44] J.S. Earl and R.A. Shenoi. Hygrothermal ageing effects on FRP laminate and structural foam materials. *Composites Part A: Applied Science and Manufacturing*, 35(11):1237–1247, 11 2004. ISSN 1359835X. doi: 10.1016/j.compositesa.2004.04.007.